

Removal of spurious solutions encountered in Helmholtz scattering resonance computations in \mathbb{R}^d

Juan C. Araujo C.¹, Christian Engström²

Abstract

In this paper we consider a sorting scheme for the removal of spurious scattering resonant pairs in two-dimensional electromagnetic problems and in three-dimensional acoustic problems. The novel sorting scheme is based on a Lippmann-Schwinger type of volume integral equation and can therefore be applied to graded material properties as well as piece-wise constant material properties. For TM/TE polarized electromagnetic waves and for acoustic waves, we compute first approximations of scattering resonances with finite elements. Then, we apply the novel sorting scheme to the computed eigenpairs and use it to remove spurious solutions in electromagnetic and acoustic scattering resonances computations at low computational cost. Several test cases with Drude-Lorentz dielectric resonators as well as with graded material properties are considered.

Keywords:

plasmon resonance, acoustic scattering resonances, resonance modes, nonlinear eigenvalue problems, Helmholtz problem, pseudospectrum, PML, DtN, leaky modes, resonant states, quasi-normal modes

1. Introduction

The most common approach to approximate scattering resonances is to truncate the domain with a perfectly matched layer (PML) and discretize the differential equations with a finite element method. This result in approximations of the true resonances but in practice also a large number of solutions that are unrelated to the true resonances. Those *spurious eigenvalues* are a major problem in resonance computations. The origin of unphysical eigenvalues in scattering resonance computations is *spectral instability*, which is common for non-normal operators [1, 2]. Spectral instability is known to be less problematic with volume integral equations compared with formulations based on differential operators. Therefore, we proposed in [3] to use a Lippmann-Schwinger type of integral equation for removing spurious solutions in a one-dimensional setting.

In this paper, we show that it is possible to extend the approach in [3] to higher dimensions. In particular, we show that the used sorting scheme can be computed cheaply and give valuable information on the location of spurious eigenvalues. This test is motivated by spectral stability properties of the Lippmann-Schwinger formulation of the problem. The idea is then to test each computed pair and obtain a pseudospectral indicator δ . Then we sort all computed pairs from the smallest to the largest value of δ . Finally, we can choose a user defined tolerance δ_{TOL} , and

¹Department of Mathematics and Mathematical Statistics, Umeå University, MIT-Huset, 90187 Umeå, Sweden

²Department of Mathematics, Linnaeus University, Hus B, 35195 Växjö, Sweden

drop all pairs with $\delta > \delta_{TOL}$. In [3] we presented computations on several test cases for space dimension $d = 1$. The strategy was successful, but the application of the ideas presented in [3] for $d = 2, 3$ turn out to be more challenging. The effective application of the sorting scheme in higher dimensions require further considerations that are addressed in the current work. The new results confirm the efficiency of using the pseudospectral indicator δ for the removal of spurious scattering resonance pairs also in \mathbb{R}^d , $d = 2, 3$.

2. Electromagnetic and acoustic scattering resonances

Assume that $\epsilon(x, \omega) = \epsilon(x_1, x_2, \omega)$ is independent of x_3 and consider electromagnetic waves propagating in the (x_1, x_2) -plane. The x_3 -independent electromagnetic field (\mathbf{E}, \mathbf{H}) is then decomposed into transverse electric (TE) polarized waves $(E_1, E_2, 0, 0, H_3)$ and transverse magnetic (TM) polarized waves $(0, 0, E_3, H_1, H_2, 0)$ [4]. This decomposition reduces Maxwell's equations to one scalar equation for H_3 and one scalar equation for E_3 . The TM-polarized waves and the TE-polarized waves satisfy formally

$$-\Delta E_3 - \omega^2 \epsilon E_3 = 0 \quad \text{and} \quad -\nabla \cdot \left(\frac{1}{\epsilon} \nabla H_3 \right) - \omega^2 H_3 = 0, \quad (1)$$

respectively. For the scattering resonance problems, E_3 and H_3 are assumed to be locally integrable functions that satisfy an outgoing condition [5, 6].

Let the physical domain $\Omega_a \subset \mathbb{R}^d$ be an open ball of radius a with boundary Γ_a , and let $\Omega_r := \text{supp}(\epsilon - 1) \subset \Omega_a$ be the bounded domain defining the resonators. Hence, we assume that the relative permittivity ϵ in $\mathbb{R}^d \setminus \Omega_r$ is one. Furthermore, let $\Omega_r := \cup_{i=1}^N \Omega_i$ denote the union of disjoint resonators $\Omega_1, \Omega_2, \dots, \Omega_N$, satisfying $0 < \epsilon_{\min} \leq |\epsilon(x)| \leq \epsilon_{\max}$ for all $x \in \Omega_a$, as shown in Figure 1. A *scattering resonance* was in [7] defined as a complex number ω for which the Lippmann-Schwinger equation

$$T(\omega)u := u - K(\omega)u = 0 \quad (2)$$

has a non-zero solution u . The integral operator K in (2) is for TM/TE waves given by

$$\begin{aligned} TM: K(\omega)u &:= \omega^2 \int_{\Omega_r} \Phi(x, y) (\epsilon - 1) u \, dy \\ TE: K(\omega)u &:= \nabla \cdot \int_{\Omega_r} \Phi(x, y) \left(\frac{1}{\epsilon} - 1 \right) \nabla u \, dy \end{aligned}, \quad \Phi(x, y) := \begin{cases} \frac{i}{2\omega} e^{i\omega|x-y|}, & d = 1 \\ \frac{i}{4} H_0^{(1)}(\omega|x-y|), & d = 2. \end{cases} \quad (3)$$

Here, $\Phi(x, y)$ is known as the outgoing Green function in free space for the Helmholtz equation [5, 6]. Notice that while we are interested in $x \in \Omega_a$, the integration in (2) is only performed over Ω_r , since the integration over the air region $\Omega_0 := \Omega_a \setminus \Omega_r$ is zero.

The scattering resonance problem (2) is a highly non-linear eigenvalue problem, where the matrices after discretization are large and full. It is possible to accurately solve the non-linear eigenvalue problem $T(\omega)u = 0$ in \mathbb{R} using a standard laptop; see e.g. [8, 3]. However, accurate computations of eigenpairs of (2) in higher dimensions would require huge computer resources; See [9] and the discussion in Section 7.6.

Acoustic scattering resonances in \mathbb{R}^3

Sound-soft materials are characterized by the speed of sound $c(x)$ and we assume that acoustic resonators are defined by $\Omega_r := \text{supp}(c^{-2} - 1) \subset \Omega_a$. Then, the acoustic pressure u satisfies formally the Helmholtz equation

$$-\Delta u - \frac{\omega^2}{c(x)^2} u = 0, \quad (4)$$

where the outgoing condition can be expressed as u satisfying an expansion in spherical harmonics outside the open ball Ω_a [10]. Moreover, (u, ω) is a scattering resonance pair if (2) holds with

$$K(\omega)u := \omega^2 \int_{\Omega_r} \Phi(x, y) \left(\frac{1}{c(y)^2} - 1 \right) u(y) dy, \quad \Phi(x, y) = \frac{e^{i\omega|x-y|}}{4\pi|x-y|}. \quad (5)$$

Note that the acoustic problem in \mathbb{R}^d , $d = 1, 2, 3$ is analogous to TM-polarized electromagnetic waves with $\epsilon = 1/c^2$.

2.1. Alternative formulations

Understanding the resonance behavior of structures in unbounded domains is important and many different approaches have been proposed. Graded material properties are increasingly popular in applications [11] and we will therefore not consider boundary integral equations. However, boundary integral equation-based methods are a good alternative for cases with piecewise constant coefficients and not too complicated geometry [12]. The most popular method to compute resonances in \mathbb{R}^d , $d > 1$ is the finite element (FE) method with a perfectly matched layer (PML). In recent years, finite element methods based on Hardy space infinite elements (HIF) [13] and DtN maps [14] have also been proposed as strong alternatives to compute resonances in higher dimensions. For the DtN map, recent developments in computational linear algebra are a key to the high performance of the method [15, 16]. Discretization with FE of the PML and HIF formulations result in sparse matrices, and a formulation in terms of a DtN result in sparse matrices except a small dense block corresponding to the DtN map. Moreover, the PML and HIF formulations result in a standard generalized eigenvalue problem if ϵ is ω -independent and in the general case the non-linearity in ω is completely determined by $\epsilon(x, \omega)$. Hence, the PML and HIF formulations seem to have the most attractive properties of the considered methods. However, it is very important to also take into account the *spectral instability* of the formulation. Then, the picture changes completely, as discussed in the next section.

2.2. Spectral instability and pseudospectra

Let A denote an unbounded closed linear operator in a Hilbert space with domain $\text{dom } A$, spectrum $\sigma(A)$, and resolvent set $\rho(A)$. Then A exhibits high *spectral instability* if for a very small $\delta > 0$ there exist many $\omega^2 \in \mathbb{C}$ and $u \in \text{dom } A$ such that

$$\|(A - \omega^2)u\| \leq \delta \|u\| \quad (6)$$

even though ω^2 is not close to $\sigma(A)$ [17]. This is closely related to the pseudospectrum $\sigma_\delta(A)$, which is defined as the union of $\sigma(A)$ and all ω^2 in the resolvent set $\rho(A)$ for which it exists an $u \in \text{dom } A$ such that (6) holds. The generalization of those results to an operator function T is straightforward and we will in some of the numerical computations rely on the following alternative characterization of the pseudospectrum:

$$\sigma_\delta(T) = \sigma(T) \cup \{\omega \in \rho(T) : \|T^{-1}(\omega)\| > \delta^{-1}\}.$$

It is well known that PML and HIF based methods encounter high spectral instability [13, 3]. Methods based on a DtN map encounter medium spectral instability [14, 3] and integral equation-based methods encounter low spectral instability [3]. Hence, the Lippmann-Schwinger equation is in our setting the preferred method in terms of spectral stability. This will be further discussed in the paper.

2.3. Domain and material properties

In electromagnetics, the material properties of non-magnetic metals are characterized by the complex relative permittivity function ϵ , which changes rapidly at optical frequencies ω . The most common accurate material model is then the Drude-Lorentz model

$$\epsilon_{\text{metal}}(\omega) := \epsilon_\infty + \sum_{j=0}^{N_p} \frac{f_j \omega_p^2}{\omega_j^2 - \omega^2 - i\omega\gamma_j}, \quad (7)$$

where $\epsilon_\infty \geq 1$ and $f_j, \omega_p, \omega_j, \gamma_j$ are non-negative [4]. Hence, the Maxwell eigenvalue problem in the spectral parameter ω is nonlinear for metal-dielectric nanostructures. Assume that the domain of the resonators can be written in the form $\Omega_r := \cup_{i=1}^N \Omega_i$ and let χ_{Ω_m} denote the characteristic function of the subset Ω_m . For material properties that are piecewise constant in Ω_a , we assume a permittivity function in the form

$$\epsilon(x, \omega) := \sum_{m=0}^{N_r} \epsilon_m(\omega) \chi_{\Omega_m}(x), \quad x \in \Omega_a, \quad \omega \in \mathcal{D}, \quad (8)$$

where the dependencies on $\omega \in \mathcal{D} \subset \mathbb{C}$ in ϵ_m for $m = 0, 1, \dots$ are of Drude-Lorentz type (7). In addition, we will consider graded material properties, meaning that ϵ is a continuous function in x . In linear acoustics, the speed of sound c is assumed to be independent of the frequency.

3. DtN and PML based methods

In the next sections, we will describe two common approaches to compute scattering resonances and the restriction of resonance modes to a compact subset of \mathbb{R}^d . In the following, we use the notation

$$-\nabla \cdot (\rho \nabla u) - \omega^2 \eta u = 0, \quad (9)$$

where $u := E_3$, $\rho := 1$, $\eta := \epsilon$ for the TM-case and $u := H_3$, $\rho := 1/\epsilon$, $\eta := 1$ for the TE-case.

We define for $u, v \in H^1(\Omega_a)$ the forms

$$\mathfrak{a}(\omega)[u, v] := \int_{\Omega_a} \rho \nabla u \cdot \nabla \bar{v} \, dx, \quad \mathfrak{b}(\omega)[u, v] := \int_{\Omega_a} \eta u \bar{v} \, dx, \quad (10)$$

where in (10), ρ and η are functions of $\omega \in \mathcal{D}$. Let \mathcal{Z} denote the set of values ω that are zeros or poles of ϵ and set $\mathcal{D} := \mathbb{C} \setminus \mathcal{Z}$.

3.1. DtN based methods

Scattering resonances ω and quasi-normal modes u restricted to Ω_a can be determined from a problem with a Dirichlet-to-Neumann (DtN) map [18, 19, 14]. Below we present variational formulations for \mathbb{R}^d , $d = 1, 2$. Formally, (ω, u) is a scattering resonance pair if (9) holds in Ω_a and

$$\frac{\partial u}{\partial n} = \mathcal{G}(\omega)u \quad \text{on } \Gamma := \partial\Omega_a, \quad (11)$$

where $\partial u / \partial n$ is the normal derivative.

3.1.1. DtN formulation in \mathbb{R}

In one space dimension the scattering resonance problem restricted to $\Omega_a := (-a, a)$ is formally: Find a non-zero u and a complex ω such that

$$-(\rho u')' - \omega^2 \eta u = 0 \text{ for } x \in \Omega_a, \quad (12)$$

where the DtN-map at $x = \pm a$ is

$$u'(-a) = -i\omega u(-a), \quad u'(a) = i\omega u(a). \quad (13)$$

Define for $u, v \in H^1(\Omega_a)$ and $\omega \in \mathcal{D}$ the forms \mathbf{a} , \mathbf{b} as in (10), and

$$g_1(\omega)[u, v] := i\omega(u(a)\bar{v}(a) + u(-a)\bar{v}(-a)). \quad (14)$$

The nonlinear eigenvalue problem is then as follows: Find vectors $u \in H^1(\Omega_a) \setminus \{0\}$ and $\omega \in \mathcal{D}$ satisfying

$$q_1(\omega)[u, v] := \mathbf{a}(\omega)[u, v] - \omega^2 \mathbf{b}(\omega)[u, v] - g_1(\omega)[u, v] = 0, \quad (15)$$

for all $v \in H^1(\Omega_a)$. Note that (15) is a quadratic eigenvalue problem if ϵ is independent of ω and a rational eigenvalue problem for Drude-Lorentz type of materials (7).

3.1.2. DtN formulation in \mathbb{R}^2

In this subsection, we present a DtN formulation in polar coordinates (r, θ) . Let $H_\nu^{(1)}(z)$ denote the Hankel function of first kind, then the DtN operator (11) on the circle Γ_a has the explicit form

$$\mathcal{G}(\omega)u := \frac{1}{2\pi} \sum_{\nu=-\infty}^{\infty} \omega \frac{H_\nu^{(1)'}(\omega a)}{H_\nu^{(1)}(\omega a)} e^{i\nu\theta} \int_0^{2\pi} u(a, \theta') e^{-i\nu\theta'} d\theta' \quad (16)$$

and $\mathcal{G}(\omega) : H^{1/2}(\Gamma_a) \rightarrow H^{-1/2}(\Gamma_a)$ is bounded [18].

The resonance problem restricted to Ω_a is formally to find non-trivial solutions (ω, u) such that (9) and (11) with (16) holds. The theory presented in [18] can with minor changes be used in the present case to derive properties of a variational formulation of the problem.

Variational formulation: Let S denote the union of the set of zeros of $H_\nu^{(1)}(\omega a)$, $\nu \in \mathbb{Z}$, and let $\mathcal{G}_{\nu_{\max}}(\omega)$ denote the operator (11) truncated after $|\nu| = \nu_{\max}$. The eigenvalues of the truncated version of (9)-(11) are determined by the following variational problem: Find $u \in H^1(\Omega_a) \setminus \{0\}$ and $\omega \in \mathcal{D} := \mathcal{D} \setminus \{\mathbb{R}^- \cup S\}$ such that for all $v \in H^1(\Omega_a)$

$$q(\omega)[u, v] := \mathbf{a}(\omega)[u, v] - \omega^2 \mathbf{b}(\omega)[u, v] - g(\omega)[u, v] = 0, \quad (17)$$

where the forms \mathbf{a} , \mathbf{b} are defined as in (10), and

$$g(\omega)[u, v] := (\mathcal{G}_{\nu_{\max}}(\omega)u, v)_{\Gamma_a} = \sum_{\nu=-\nu_{\max}}^{\nu_{\max}} \omega a \frac{H_\nu^{(1)'}(\omega a)}{H_\nu^{(1)}(\omega a)} \hat{u}_\nu \bar{\hat{v}}_\nu, \quad \hat{\varphi}_\nu = \frac{1}{\sqrt{2\pi}} \int_0^{2\pi} \varphi(a, \theta) e^{-i\nu\theta} d\theta. \quad (18)$$

3.2. PML based methods

In the previous section, a DtN-map was used to reduce the exterior Helmholtz problem to a bounded domain. In this section, we consider an alternative approach based on a complex coordinate stretching (the PML method), which results in a linear eigenvalue problem for non dispersive material coefficients [20]. The method consists on attaching to Ω_a a buffer layer of thickness ℓ , where outgoing solutions decay rapidly. The buffer domain is referred to as Ω_{PML} and the full computational domain $\Omega := \Omega_a \cup \Omega_{PML}$ is enlarged as shown in the Figure 1.

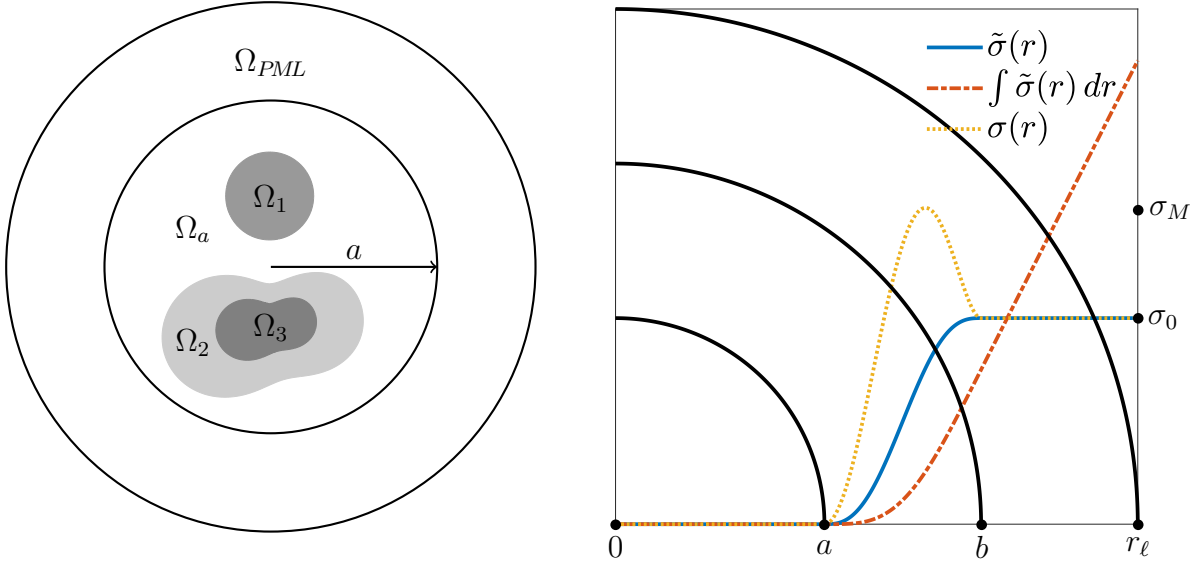


Figure 1: Left) Arbitrary configuration of resonators. Right) PML stretching function.

3.2.1. PML formulation in \mathbb{R}

Let $\ell > 0$, $r = |x|$, and $0 < a < b < r_\ell$, with $r_\ell = b + \ell$. The action of the PML is defined through the stretch function

$$\tilde{\sigma}(r) := \begin{cases} 0, & \text{if } r < a \\ P(r), & \text{if } a \leq r \leq b \\ \sigma_0, & \text{if } r > b \end{cases} \quad (19)$$

where the polynomial $P(r)$ is required to be increasing in $[a, b]$, and $\tilde{\sigma} \in C^2(0, r_\ell)$. Here, we use the fifth order polynomial $P(r)$ satisfying: $P(a) = P'(a) = P''(a) = P'(b) = P''(b) = 0$ and $P(b) = \sigma_0$.

The PML problem is restricted to $(-r_\ell, r_\ell)$ and the PML strength function has then the profile shown in Figure 1. In the following sections, we consider the complex change of variable and transformation rule

$$\tilde{x} = \int_{x_0}^x \tilde{\alpha}(y) dy, \quad \frac{d}{d\tilde{x}} = \frac{1}{\tilde{\alpha}(x)} \frac{d}{dx}, \quad \text{with } \tilde{\alpha}(x) = 1 + i\tilde{\sigma}(x), \quad (20)$$

where $x_0 = -\infty$ in \mathbb{R}^- and $x_0 = a$ in \mathbb{R}^+ .

For finite element computations we restrict the domain to $\Omega_\ell := (-r_\ell, r_\ell)$, define $\Omega_{PML} = (-r_\ell, -a) \cup (a, r_\ell)$, and choose as in [20] homogeneous Dirichlet boundary conditions. Formally, the *finite PML problem* is then: Find the eigenpairs (ω, u) such that

$$-\frac{d}{dx} \left(\frac{\rho}{\tilde{\alpha}} \frac{du}{dx} \right) - \omega^2 \eta \tilde{\alpha} u = 0, \quad x \in \Omega_\ell, \quad u(r_\ell) = 0 \quad \text{and} \quad u(-r_\ell) = 0. \quad (21)$$

In the following, we consider a variational formulation of (21).

Find $u \in H_0^1(\Omega_\ell) \setminus \{0\}$ and $\omega \in \mathcal{D} := \mathbb{C} \setminus \mathcal{Z}$ such that for all $v \in H_0^1(\Omega_\ell)$

$$t_1(\omega)[u, v] := \mathbf{a}(\omega)[u, v] - \omega^2 \mathbf{b}(\omega)[u, v] + \hat{t}_1(\omega)[u, v] = 0, \quad (22)$$

where $\hat{t}_1(\omega)[u, v] = (\frac{1}{\tilde{\alpha}} u', v')_{\Omega_{PML}} - \omega^2 (\tilde{\alpha} u, v)_{\Omega_{PML}}$, and the forms \mathbf{a} , \mathbf{b} are defined as in (10).

3.2.2. PML formulation for \mathbb{R}^d

Approximation of scattering resonances using a radial PML was analyzed in [20] and we will here only consider the PML problem truncated to the ball $\Omega \subset \mathbb{R}^d$, $d = 2, 3$. The used complex stretching functions are as in one-dimension of the form (19). Let $\Omega := \Omega_a \cup \Omega_{PML}$ denote a partition into the PML-region and the part of the domain Ω_a containing the resonators.

In the sequel we need the following definitions

$$\begin{aligned}\tilde{\alpha}(r) &:= 1 + i\tilde{\sigma}(r), & \tilde{r}(r) &:= (1 + i\tilde{\sigma})r = \tilde{\alpha}(r)r, \\ \sigma(r) &:= \tilde{\sigma}(r) + r \frac{\partial \tilde{\sigma}}{\partial r}, & \alpha(r) &:= \frac{\partial \tilde{r}}{\partial r} = 1 + i\sigma(r),\end{aligned}\tag{23}$$

with the properties $\sigma(r) = \partial(r\tilde{\sigma})/\partial r$ and $\alpha(r) = \tilde{\alpha}(r) = 1 + i\sigma_0$ for $r > b$.

It is clear that the PML coefficients are designed such that for $r \leq a$, we obtain $\sigma(r) = 0$ and $\alpha(r) = 1$. Hence, the PML operator restricted to $r \leq a$ corresponds to the original operator in problem (9) (no PML effect).

Variational formulation: The eigenvalues of (9) with radial PML are then determined by the following variational problem: Find $u \in H_0^1(\Omega) \setminus \{0\}$ and $\omega \in \mathcal{D} := \mathbb{C} \setminus \mathcal{Z}$ such that for all $v \in H_0^1(\Omega)$

$$t(\omega)[u, v] := \mathbf{a}(\omega)[u, v] - \omega^2 \mathbf{b}(\omega)[u, v] + \hat{t}(\omega)[u, v] = 0,\tag{24}$$

where $\hat{t}(\omega)[u, v] := (\mathcal{A}\nabla u, \nabla v)_{\Omega_{PML}} - \omega^2 (\mathcal{B}u, v)_{\Omega_{PML}}$, and the forms \mathbf{a} , \mathbf{b} are defined as in (10).

For $d = 2$, a direct transformation of (24) from polar to Cartesian coordinates results in

$$\mathcal{A} = \begin{pmatrix} \frac{\tilde{\alpha}}{\alpha} \cos^2 \theta + \frac{\alpha}{\tilde{\alpha}} \sin^2 \theta & \left(\frac{\tilde{\alpha}}{\alpha} - \frac{\alpha}{\tilde{\alpha}} \right) \sin \theta \cos \theta \\ \left(\frac{\tilde{\alpha}}{\alpha} - \frac{\alpha}{\tilde{\alpha}} \right) \sin \theta \cos \theta & \frac{\tilde{\alpha}}{\alpha} \sin^2 \theta + \frac{\alpha}{\tilde{\alpha}} \cos^2 \theta \end{pmatrix}, \quad \mathcal{B} := \alpha \tilde{\alpha}.\tag{25}$$

Even though \mathcal{A} , and \mathcal{B} are defined in the whole Ω , their action takes place only in Ω_{PML} . In the case $d = 3$, the PML is set up similarly as done in [21].

4. Discretization of the Lippmann-Schwinger equation

In this section we present a collocation method for discretization of the Lippmann-Schwinger equation (2), which will be used to compute resonances in one-dimension and it is the base for the numerical sorting algorithm in Section 6. Further computational details are given in Section 7.6.

4.1. A Galerkin-Nyström method

We present a Galerkin-Nyström discretization method for linear Fredholm integral equations of the second kind, with kernels satisfying $\int_D \int_D |\Phi(x, y)|^2 dx dy < \infty$ for x, y in the compact set $D \subset \mathbb{R}^d$. In [22], this method is referred to as case (A) of the Galerkin methods, and convergence for the problem with sources is discussed.

Let $\{\varphi_j\}_{j=1}^N$ be piecewise polynomial functions with the property $\varphi_j(x_i) = \delta_{ji}$, $\{x_i\}_{i=1}^N \in \Omega_a$ and set $u^\gamma = \sum_j^N \xi_j \varphi_j$. Then, with the use of (2) we obtain the nonlinear eigenvalue problem: Find $\xi \in \mathbb{C}^N$ and $\omega^\gamma \in \mathbb{C}$ such that

$$T^\gamma(\omega^\gamma)\xi = (I - K(\omega^\gamma))\xi = 0, \quad \text{with}$$

$$\begin{aligned}TM : \quad K_{ij}(\omega) &:= \omega^2 \int_{\Omega_r} \Phi(x_i, y) (\epsilon - 1) \varphi_j dy, \\ TE : \quad K_{ij}(\omega) &:= \nabla \cdot \int_{\Omega_r} \Phi(x_i, y) \left(\frac{1}{\epsilon} - 1 \right) \nabla \varphi_j dy,\end{aligned}\tag{26}$$

The Nyström method consists in choosing the collocation points x_i as the nodes of a high order quadrature rule. By doing this, the convergence of the scheme is considerably improved. In Section 7.6 we describe some of the implementation details of the Galerkin-Nyström discretization.

The resulting nonlinear matrix eigenvalue problem (26) is in this paper solved by using a contour integration based method [23, 24, 25].

Remark 1. *The formulation in (2) uses information of the exact solution of the problem at every discretization node x_i , through its fundamental solution $\Phi(x, y)$. The numerical scheme is flexible in the sense that it can be posed in the smallest domain Ω_r , as well as in larger domains $\Omega \supset \Omega_r$, without any special handling of the boundary conditions.*

5. FE discretization of the DtN and PML based formulations

In this section we discuss briefly the details involved in the assembly of the matrices corresponding to the discretization of the formulations given in (2) and in (9).

5.1. Discretization with the finite element method

Let the domain $\Omega \subset \mathbb{R}^d$ be covered with a regular and quasi uniform finite element mesh $\mathcal{T}(\Omega)$ consisting of elements $\{K_j\}_{j=1}^N$. The mesh is designed such that the permittivity function ϵ is continuous in each K_j . Let h_j be the length of the largest diagonal of the non-curved primitive K_j and denote by h the maximum mesh size $h := \max_j h_j$.

Let \mathcal{P}_p denote the space of polynomials on \mathbb{R}^d of degree $\leq p$ and define the N dimensional finite element space

$$S^\gamma(\Omega) := \{u \in H^1(\Omega_a) : u|_{K_j} \in \mathcal{P}_p(K_j) \text{ for } K_j \in \mathcal{T}\}. \quad (27)$$

The computations of discrete resonance pairs $(u^\gamma, \omega^\gamma)$ are for $d = 2, 3$ performed in the approximated domain Ω^γ using curvilinear elements [26]. The meshes used are *shape regular* in the sense of [27, Sec. 4.3], and consist of quadrilateral/brick elements with curvilinear edges/surfaces that deviate slightly from their *non-curved* primitives.

5.2. Assembly of the FE matrices

In this section we refer to domains $\Omega_q \subset \mathbb{R}^d$. Let $\{\varphi_1, \dots, \varphi_N\}$ be a basis of $S^\gamma(\Omega^\gamma)$. Then $u_\gamma \in S^\gamma(\Omega^\gamma)$ and the entries in the finite element matrices are of the form

$$u_\gamma = \sum_{j=1}^N \xi_j \varphi_j, \quad A_{ij} = (\rho \nabla \varphi_j, \nabla \varphi_i)_{\Omega_a^\gamma}, \quad M_{ij} = (\eta \varphi_j, \varphi_i)_{\Omega_a^\gamma}. \quad (28)$$

The matrix eigenvalue problem is then: Find the eigenpairs $(\omega, \xi) \in \mathcal{D} \times \mathbb{C}^N \setminus \{0\}$ such that

$$F(\omega) \xi := (A - \omega^2 M + Q)(\omega) \xi = 0, \quad (29)$$

where the corresponding matrix valued function is

$$Q_{ij}(\omega) := \begin{cases} -g_1(\omega)[\varphi_j, \varphi_i], & \text{DtN and } d = 1 \\ -g(\omega)[\varphi_j, \varphi_i], & \text{DtN and } d = 2 \end{cases}, \text{ or } \begin{cases} \hat{t}_1(\omega)[\varphi_j, \varphi_i], & \text{PML and } d = 1 \\ \hat{t}(\omega)[\varphi_j, \varphi_i], & \text{PML and } d = 2, 3 \end{cases}. \quad (30)$$

In the case where $\epsilon(\omega, x)$ is given as a piecewise smooth function of space, we write (29) as

$$F(\omega) \xi := \left(\sum_{m=0}^{N_r} \{ \rho_m(\omega) \tilde{A}_m - \omega^2 \eta_m(\omega) \tilde{M}_m \} + Q(\omega) \right) \xi = 0, \quad (31)$$

with matrices $\tilde{A}_{ij}^m = (\nabla \varphi_j, \nabla \varphi_i)_{\Omega_m^\gamma}$, $\tilde{M}_{ij}^m = (\varphi_j, \varphi_i)_{\Omega_m^\gamma}$, $m = 0, 1, \dots, N_r$.

Remark 2. Truncation of the DtN: Let $\lceil z \rceil$ be the smallest integer greater than or equal to z . We use the rule $\nu_{\max} = \lceil a \omega_M \rceil$ as suggested in [14], where from the considered spectral window ω_M is the largest real part for computations of eigenvalues.

Remark 3. Truncation of the PML: The PML is set up following the discussions in [20, 3], which accounts for large enough ℓ and σ_0 such that the search region is feasible. Additionally, we use the space $S_0^\gamma(\Omega) := \{u \in S^\gamma(\Omega) : u = 0 \text{ for } x \in \partial\Omega^\gamma\}$ for computations with the PML formulation.

Remark 4. All formulations (LS, DtN, PML) use the FE triangulation $\mathcal{T}(\Omega_a)$, which is the restriction of $\mathcal{T}(\Omega)$ to Ω_a . This ensure that the approximation properties in the physical domain are the same for all formulations.

6. Numerical sorting of resonances

In this section, we derive a discrete form of (2) that allow us to identify resonances from spurious solutions once we have computed FE solutions $(\omega_m^\gamma, u_m^\gamma)$ to (29) or to (31). The resulting expression for the sorting scheme is a discrete form of the condition $\|\chi_a T(\omega) \chi_a u\| < \delta$, where u^γ is a FE solution restricted to Ω_a . Let $\{\varphi_j\}$ be a basis for $S^\gamma(\Omega_a)$ and let P^γ be the L_2 -projection on $S^\gamma(\Omega_a)$. Then, the discrete Lippmann-Schwinger equation (26) is written in the form

$$T(\omega) u^\gamma = u^\gamma - K(\omega) u^\gamma, \quad u^\gamma := \sum_{j=1}^N \xi_j \varphi_j, \quad \text{with } \|u^\gamma\|_{L^2(\Omega_a)} = 1.$$

Definition 5. Pseudospectrum indicator: The computed eigenvalue ω^γ belongs, for given $\delta > 0$, to the δ -psudospectrum $\sigma_\delta(T^\gamma)$ if the pair $(\omega^\gamma, u^\gamma)$ satisfies $\|T^\gamma(\omega^\gamma) u^\gamma\|_{\Omega_a} < \delta$. Then, for a given domain $\Omega_a \supseteq \Omega_r$, we define the pseudospectrum indicator as

$$\delta^\gamma(\Omega_a) := \|T^\gamma(\omega^\gamma) u^\gamma\|_{\Omega_a}. \quad (32)$$

We aim to measure whether or not the computed eigenpair $(\omega^\gamma, u^\gamma)$ is related to a physical scattering resonance pair, but naturally, very bad approximations exhibit also large δ^γ values.

Additionally, spurious eigenpairs introduced by using the PML method are easily identified and can be removed by using (33) in the following definition.

Definition 6. PML added eigenpairs: The use of the coordinate stretching technique in formulations (22), (24) introduces new eigenpairs to problem (9). These new eigenvalues accumulate close to the critical line of the modified PML problem [3], and eigenfunctions v_m exhibit oscillations in Ω_{PML} , but decay in the physical region Ω_a . Then, by using the normalization $\|v_m\|_{L^2(\Omega)} = 1$, the PML critical eigenvalues exhibit

$$0 < \frac{\|v_m\|_{L^2(\Omega_a)}}{|\Omega_a|} < \frac{\|v_m\|_{L^2(\Omega_{PML})}}{|\Omega_{PML}|}, \quad (33)$$

which can be succesfully used as a filtering criterion for removing PML added eigenpairs.

7. Computational details

In this section we outline the computational details for the FE discretization of the DtN and PML based formulations in Section 5. Furthermore, we present results on integration of weakly singular kernels that are used in the new numerical sorting scheme in Subsection 7.7. For convenience of the reader we provide a summary of the used standard techniques.

7.1. Master element and transfinite interpolation

Consider a physical element K and let $\mathcal{K} := (-1, 1)^d$ denote the master element. Numerical quadrature is used to integrate a function over K and when high order polynomial spaces are used, it is convenient to compute information from the shape functions φ_j , $\nabla\varphi_j$ in the master element \mathcal{K} and then store it. In this way we gain in performance as computations from high polynomials are expensive. Consequently, functions defined over a physical element K are mapped to functions over \mathcal{K} , where we perform integration. Then, the mapping $X_K : \mathbb{R}^d \rightarrow \mathbb{R}^d$ transforms coordinates as $K = X_K(\mathcal{K})$. The action of the mapping is enforced by the Jacobian's determinant $J = \det(DX_K)$ [28, Sec. 3.3], [29, Sec. 3.4]. Then, we have

$$\int_K f(x) dx = \int_{\mathcal{K}} f \circ X_K(y) J(y) dy. \quad (34)$$

For the case where K is a line, quadrilateral or a brick element, the explicit expression for $X_K(\mathcal{K})$ is a known bilinear transformation. When K has curved edges, $X_K(\mathcal{K})$ can be described by the theory of Transfinite Interpolation [30], and the implementation and computational details can be found in [31], [29, Sec. 3.2]. A general rule of thumb is that the bending of the edges must be small compared to the diameter of the element, and that the angles at the element corners should be close to $\pi/2$. For further details and explicit error estimates on curved elements the reader is referred to [28, Sec. 3.3], [32, Sec. 6.7]. For the description on how φ_j , $\nabla\varphi_j$ transform from K to \mathcal{K} , and other related details, the reader is referred to [29, Sec. 3.3].

7.2. Evaluation of integrals

In this subsection, we revise briefly numerical integration by *Gaussian-Legendre* quadratures. In the one dimensional case, integration over the master element is approximated by formulas of the form $\int_{\mathcal{K}} f(x) dx = \sum_{i=1}^m w_i f(x_i) + E$, where w_i are the quadrature weights, x_i the quadrature nodes, and E is the quadrature error or remainder. The coefficients w_i are all positive [33, Sec. 8.4]. These type of quadrature rules are derived under the assumption that $f \in C^{2m}(\mathcal{K})$, $m \in \mathbb{N}$. Then, the Weierstrass approximation theorem [33, Sec 1.2] guarantees the existence of a polynomial $P(x)$ such that $\sup_{x \in \mathcal{K}} |f(x) - P(x)| \leq \delta$, for a specified $\delta > 0$. In this way w_i, x_i can be set to minimize E , and $P(x)$ is integrated exactly. The effective way of reducing $\sup_{x \in \mathcal{K}} |f(x) - P(x)|$ is by increasing the polynomial degree p until the residual is below δ . In the quadrature formula, increasing p is equivalent to increasing the number of evaluation points m . The remainder for the m -point Gaussian quadrature satisfies

$$|E| \leq C |f^{(2m)}(\xi)|, \text{ for } \xi \in \mathcal{K}, \quad (35)$$

where we see that if f is a polynomial of order $p < 2m$, the remainder vanishes and the quadrature gives the exact integral value. Further details on Gaussian quadratures can be revised in e.g. [33, Ch. 8], and implementation details are provided in [34, Ch 4].

In \mathbb{R}^d , $d > 1$, we describe quadrature formulas for integration of $f \in C^{2m}(\mathcal{K})$, when a physical element K is allowed to be curved. Then, we resource to the formula

$$\int_K f(x) dx = \int_{\mathcal{K}} f \circ X_K(y) J(y) dy = \sum_{j=1}^{m^2} w_j f(x_j) + E(K), \quad (36)$$

where the new weights and nodes w_j, x_j are the piled up tensor product version of vector of the corresponding one dimensional values. For example, with $d = 2$, and $i, j = 1, 2, \dots, m$, the new index is $k = (i - 1)m + j$, and $y_k = [y_i, y_j]^T$. Then, we obtain the transformed nodes $x_k = X_K(y_k)$ and the corresponding weights as $w_k = w_i w_j J(y_k)$.

Finally, we discuss the composite of a quadrature rule, when integration is performed over a domain $\Omega \supseteq \cup_i K_i$ defined by the union of several elements K_i . The integrand is now required to be piecewise smooth $f \in C^{2m}(K_i)$, for $i = 1, 2, \dots, N_{\text{elements}}$. Then, we obtain

$$\int_{\Omega} f(x) dx = \sum_i \int_{K_i} f(x) dx = \sum_i \sum_k w_k(K_i) f(x_k(K_i)) + E(\Omega), \quad (37)$$

where for each element K_i , we have the quadrature pairs $x_k(K_i), w_k(K_i)$, similarly as in (36).

The polynomial spaces that we use for $d = 2, 3$ are based on the tensor product of one dimensional finite element spaces [34, Sec. 2.2], [35]. As the coefficients are piecewise smooth, we make sure that the jumps of f coincide with the possibly curved element edges ∂K_i , such that for $x \in K_i$ we have $f \in C^{2m}(K_i)$. This allow us to use quadrature rules in each individual element and guarantee convergence of the error of the numerical integration.

7.2.1. Integrating weakly singular kernels

In the discretization of the Lippmann-Schwinger formulation (26), we encounter the situation where the integrand contain both evaluation points x, y in an element $K_l \subset \Omega_r$. For one-dimensional problems ($d = 1$), the kernel $\Phi(x, y)$ is continuous, but has a jump in the derivative at points $x = y$. In the troublesome element $K_l := (x_l, x_{l+1})$, we can always split the integration interval $K_l \rightarrow (x_l, x_j) \cup (x_j, x_{l+1})$ and perform two separate quadrature integrations. Then, by using Gauss-type of quadratures, it is possible to avoid the evaluation of $\Phi(x_j, x_j)$ [3].

In higher dimensions ($d = 2, 3$) the kernel is weakly singular [36, Sec. 2.3], which makes the integration in (26) more demanding. This difficulty can be overcome by specializing the quadratures as done for example in [37], [38], and [39]. There, extra effort was spent in refining adaptively on elements K_l , where the integrand is unbounded. Then a Nyström type of high order quadratures, combined with interpolation in polar coordinates along with other techniques were used in order to keep $E(\Omega_r)$ small to desired order. As expected, the challenge becomes more pronounced in higher dimension as can be seen in [38] and in [39]. In those papers the aim was to solve a scattering problem through the Lippmann-Schwinger formulation for a given incoming wave. However, our case is very different as we look for scattering resonances, where the corresponding eigensolver is computationally much more demanding than a linear solve.

7.3. Solution of the nonlinear eigenvalue problems

The approximation of resonances based on the DtN formulation for $d = 2$ leads to the matrix problem in (29). The solution of this NEP is based on the solution strategy presented in [14], where we use a specialization of the Infinite Arnoldi method [40, 41] called the tensor infinite Arnoldi

d	p	m	n_c	N_z^S	N_z^D	$W^S(\text{bytes})$	$W^D(\text{bytes})$
1	2	10	10^1	9.0×10^1	4.0×10^2	1.4×10^3	6.4×10^3
2	2	10	10^2	8.1×10^3	1.6×10^5	1.3×10^5	2.6×10^6
3	2	10	10^3	7.3×10^5	6.4×10^7	1.2×10^7	1.0×10^9
1	2	10^2	10^2	9.0×10^2	4.0×10^4	1.4×10^4	6.4×10^5
2	2	10^2	10^4	8.1×10^5	1.6×10^9	1.3×10^7	2.5×10^{10}
3	2	10^2	10^6	7.3×10^8	6.4×10^{13}	1.2×10^{10}	1.0×10^{15}
1	2	10^3	10^3	9.0×10^3	4.0×10^6	1.4×10^5	6.4×10^7
2	2	10^3	10^6	8.1×10^7	1.6×10^{13}	1.3×10^9	2.6×10^{14}
3	2	10^3	10^9	7.3×10^{11}	6.4×10^{19}	1.2×10^{13}	1.0×10^{21}

Table 1: *Memory consumption estimation for matrices in (29), and (26) for $d = 1, 2, 3$.*

method (TIAR). In particular we introduce a pole cancellation technique in order to increase the radius of convergence for computation of eigenvalues that lie close to the poles of the matrix-valued function.

For the approximation of resonances with the rational permittivity function (7), we solve the corresponding matrix NEP by the techniques presented in [42], which is a specialization of the solver in [43] implemented in the SLEPc library [44].

7.4. Properties of volume integral equations for resonance computation

We discretize *volume* integral equations by using the scheme presented in (26). In Section 8.2 we will numerically show the desired stability of the spectrum of the resulting discrete operator function T for perturbations of the radius a .

Remark 7. *The resulting system matrices for T has dimensions comparable to FE matrices: $N_l \times N_l$, with $N_l \leq ch^{-d}$. However, the matrices are dense ($\mathcal{O}(N_l^2)$ storage), non-symmetric, and the elements of $T(\omega)$ are transcendental functions of ω .*

The consequences of Remark 7 in a NEP solution strategy is that the matrix $T(\omega_j)$ from (26) must be re-assembled for each new iteration $\omega_{j+1} = \omega_j + \delta\omega$, which is very expensive especially for problems of dimension $d > 1$.

7.5. Memory requirements

Let n_c be the number of cells in a triangulation in space dimension d , and let p denote the polynomial degree of the basis functions in use. Given the number of non zeros elements N_z in a matrix, the memory required to store it is $W = N_z \times w$, where $w = 16$ bytes is the memory required to store a complex number in double precision.

In the collocation method given in Section 4.1, matrices are dense, and we get $N_z^D \approx [n_c \times p^d]^2$. In turn, the FE matrices from Section 5.2 are sparse, and each cell in the triangulation contributes with a block of size $[(p+1) \times (p+1)]^d$ support points. Additionally, we have scattered connections of order $(p+1)^d$ with neighboring cells, but that contribution is omitted for simplicity. A simple estimation gives $N_z^S \approx n_c \times (p+1)^{2d}$. Furthermore, by assuming a one-dimensional partition with m divisions, the number of cells in higher dimensions is of the order $n_c \approx m^d$. We use for our estimations $m = 10, 10^2, 10^3$ for small, moderate, and large problems.

In Table 1, we list our estimations of the memory consumption for the FE discretization methods 5.2 and the collocation methods in Section 4.1 when $p = 2$. As expected, the sparse FE matrices are even for $d = 3$ manageable with current computer memory constraints. For the discretization of the volume integral equation (26), we conclude that storage becomes computationally unfeasible in higher space dimensions even for $p = 2$. In [7, Sec. 3.2] the method in Section 4.1 was used for resonance computations in thin structures, with an effective equation in $d = 1$. The case $d = 2$ was considered in [9], but the large problem size forced them to consider only coarse discretizations of the lowest frequency resonances.

7.6. Computational platform and details

All numerical experiments have been carried out using the finite element library *deal.II* [35] with Gauss-Lobatto shape functions [34, Sec. 1.2.3]. For fast assembly and computations with complex numbers the package PETSc [45] is used.

The computational platform was provided by the High-Performance Computing Center North (HPC2N) at Umeå University, and all experiments were run on the distributed memory system Abisko. The jobs were run in serial on an exclusive node: during the process, no other jobs were running on the same node. Node specifications: four AMD Opteron 6238 processors with a total of 48 cores per node.

7.7. Computational details of the sorting scheme

In order to evaluate the sorting scheme, we are interested in computing the integrals from (26) as accurately as possible. The available FE machinery for computing integrals over Ω_0 , facilitates the numerical integration, which is done similarly as described in Section 7.2.

Due to the growth of most resonant modes, the point-wise residual $|(T^\gamma(\omega^\gamma)u^\gamma)(x_j)|$ is expected to be larger for $x_j \in \Omega_a$. Additionally, as discussed in Section 7.2.1, due to the unboundedness of $\Phi(x_j, x_j)$, the computation of (26), and (32) for $x_j \in \Omega_r$ requires considerable more effort compared to its evaluation for $x_j \in \Omega_0$. The apparent reason for this is that for $x_j \in \Omega_r$ and $d > 1$, we have to numerically compute an integral with a weak singularity, which we discuss further in Section 7.2.1.

Below, we present explicitly the steps involved in computing $\delta^\gamma(\Omega_a)$ in Definition 5. First, we split the integration into separate parts over Ω_0, Ω_r and use the composite quadrature rules (37) for evaluating the integrals. We need the following definitions.

Definition 8. Let $\mathcal{K}_0 := \{i : K_i \subset \Omega_0\}$ and $\mathcal{K}_r := \{i : K_i \subset \Omega_r\}$ be index sets defined over Ω_0 and Ω_r , respectively. Define the sets $\mathcal{X}_0 := \cup_{i \in \mathcal{K}_0} \{x_j \in K_i\}_{j=1}^{m^2}$, $\mathcal{X}_r := \cup_{i \in \mathcal{K}_r} \{x_j \in K_i\}_{j=1}^{m^2}$, and denote by $\mathcal{I}_0, \mathcal{I}_r$ the resulting extracted index sets from the new ordering.

Using the definitions above, we have

$$\begin{aligned} \delta^\gamma(\Omega_a)^2 &= \|T^\gamma(\omega^\gamma)u^\gamma\|_{\Omega_a}^2 \\ &= \int_{\Omega_0} |(T^\gamma(\omega^\gamma)u^\gamma)(x)|^2 dx + \int_{\Omega_r} |(T^\gamma(\omega^\gamma)u^\gamma)(y)|^2 dy \\ &= \sum_{l \in \mathcal{K}_0} \sum_j w_j \alpha_{lj}^2 + \sum_{m \in \mathcal{K}_r} \sum_j w_j \beta_{mj}^2 + E(\Omega_0) + E(\Omega_r), \end{aligned} \tag{38}$$

where $\alpha_{lj} := |(T^\gamma(\omega^\gamma)u^\gamma)(x_j(K_l))|$, $\beta_{mj} := |(T^\gamma(\omega^\gamma)u^\gamma)(y_j(K_m))|$, for $x_j \in \Omega_r, y_j \in \Omega_0$. From (26), the evaluation of $T(\omega)u$ involves an integration over Ω_r , which we refer to as *inner loop*. Then, for each j in α_{lj}, β_{mj} we compute an inner loop, which is added to the explicit integration shown in (38).

d	p	m	n_r	cost	$t_i(s)$	$t(s)$
1	2	10^1	10^1	1.8×10^3	9.0×10^{-5}	1.8×10^{-3}
2	2	10^1	10^2	3.2×10^6	8.1×10^{-3}	3.2×10^0
3	2	10^1	10^3	5.8×10^9	7.3×10^{-1}	5.8×10^3
1	2	10^2	10^2	1.8×10^5	9.0×10^{-4}	1.8×10^{-1}
2	2	10^2	10^4	3.2×10^{10}	8.1×10^{-1}	3.2×10^4
3	2	10^2	10^6	5.8×10^{15}	7.3×10^2	5.8×10^9
1	2	10^3	10^3	1.8×10^7	9.0×10^{-2}	1.8×10^2
2	2	10^3	10^6	3.2×10^{14}	8.1×10^1	3.2×10^8
3	2	10^3	10^9	5.8×10^{21}	7.3×10^5	5.8×10^{15}

Table 2: Cost and time estimation for computing (38) for $d = 1, 2, 3$.

7.7.1. Computational costs

In this subsection, we estimate the computational cost for performing the operations involved in (38). Computationally, the errors in (38) require special treatment as discussed in Section 7.2.1. However, for simplicity of the estimations, we disregard additional costs from integration of weakly singular kernels in higher dimensions.

We estimate the costs in terms of the evaluation of $u^\gamma(x_j)$ and $\Phi(x_i, x_j)$ in complex double precision, which combined account for the heaviest work load in each individual term of (38). The evaluation of these two operations accounts for a computational time of around $t_q \approx 10^{-6}s$ on the processor Intel Core i7-3770, CPU: 3.40GHz.

For the estimation, we let n_c denote the number of cells $K_i \subset \Omega_a$ and choose a finite element space of degree p . Then, we have $n_c \times (p+1)^d$ terms in the outer loop, and the inner loop requires $n_r \times (p+1)^d$ terms, where n_r denotes the number of cells in Ω_r . Hence, computing $\|T^\gamma(\omega^\gamma)u^\gamma\|_{\Omega_a}^2$ costs about $n_c \times (p+1)^d \times n_r \times (p+1)^d = n_c \times n_r \times (p+1)^{2d}$ evaluations of the kernel.

Let m denote the size of a one-dimensional partition, in higher dimensions n_r, n_c are of the order $n_r \approx m^d, n_c \approx (cm)^d$, for $c > 1$. Then, the cost is given by $c^d \times (m \times (p+1))^{2d}$, which becomes prohibitively expensive for higher dimensions. As an illustration, we consider estimations of the cost, inner time t_i , and total time t for a single processor. We use $c = 2$, and $m = 10, 10^2, 10^3$ for a small, moderate and large problem, respectively. In Table 2 we show the estimations for the computational costs and times required by (38), with the aim of getting a better understanding of the requirements of the computation.

The presented sorting scheme is fully parallelizable, and the total time of execution can be reduced by a factor of ten by using additional cores. However, the conclusion of Table 2 is that the computational cost is extremely high for realistic computations. Basically, evaluating $\delta_m^\gamma(\Omega_a)$ as in (32) results in sorting schemes that are far more expensive than the solution of the NEP (29).

7.7.2. Sorting strategy

A pseudospectrum strategy based on Definition 5, consists of sorting the computed solution pairs (ω_m^γ, ξ_m) of (29), according to their respective indicator $\delta_m^\gamma(\Omega_a)$. As discussed in Section 7.2.1, the evaluation of the β_{mj} in (38) requires special treatment such as non-standard quadrature rules similar to the ones introduced in [37, 38, 39]. Additionally, the estimations presented in Table 2, show that the evaluation of $\delta_m^\gamma(\Omega_a) := \|u_m - Ku_m\|_{L^2(\Omega_a)}$ in higher dimensions is prohibitively expensive because Ku_m is a volume integral operator. With these issues in mind, our aim is to

propose an approximated version of $\delta^\gamma(\Omega_a)$ from Definition 5 such that we improve in performance compared to the results in Table 2, and we avoid the use of specialized quadrature schemes for the evaluation of singular kernels. Then, our goal is to reduce the complexity of the sorting scheme, such that the new strategy becomes at most as expensive as the computation of the inner loop, which is a reasonable price to pay.

In the remaining of the section, we present an alternative sorting algorithm based on Definition 5 with computational cost that scales with the cost of evaluating the inner loop.

7.7.3. Sorting estimations

The definitions given in Def. 8 are used to order quadrature pairs over elements, into two ($q = 0, r$) final quadrature collections that we write as

$$\{\mathbf{x}_k^q\} := \cup_{i \in \mathcal{K}_q} \{\mathbf{x}_j(K_i)\}_{j=1}^{m^2} \quad \text{and} \quad \{\mathbf{w}_k^q\} := \cup_{i \in \mathcal{K}_q} \{\mathbf{w}_j(K_i)\}_{j=1}^{m^2}.$$

Then, from the Definition 5 and (38) we have

$$\begin{aligned} \delta^\gamma(\Omega_a)^2 &= \|T^\gamma(\omega^\gamma)u^\gamma\|_{\Omega_a}^2 \\ &\approx \sum_{l \in \mathcal{K}_0} \sum_j \mathbf{w}_j \alpha_{lj}^2 + \sum_{m \in \mathcal{K}_r} \sum_j \mathbf{w}_j \beta_{mj}^2 \\ &\leq \max_{l \in \mathcal{I}_0} (\alpha_l)^2 \sum_{j \in \mathcal{I}_0} \mathbf{w}_j^0 + \max_{m \in \mathcal{I}_r} (\beta_m)^2 \sum_{j \in \mathcal{I}_r} \mathbf{w}_j^r \\ &= \max_{l \in \mathcal{I}_0} (\alpha_l)^2 \cdot |\Omega_0| + \max_{m \in \mathcal{I}_r} (\beta_m)^2 \cdot |\Omega_r|, \end{aligned} \tag{39}$$

where $\alpha_l := |(T^\gamma(\omega^\gamma)u^\gamma)(x_l)|$, $x_l \in \mathcal{X}_0$, and $\beta_m := |(T^\gamma(\omega^\gamma)u^\gamma)(x_m)|$, $x_m \in \mathcal{X}_r$. In the estimate (39), we used the properties that the quadrature weights \mathbf{w}_m are positive, and that $|\Omega| = \int_\Omega dx = \sum_i \mathbf{w}_i + E(\Omega)$.

The estimate (39) suggests an alternative strategy for approximating the pseudospectrum indicator in Definition 5. The result is an effective and inexpensive way of testing the computed pair (ω^γ, ξ) , where the cost scales linearly with the inner loop. We base our sorting strategy on the following definition.

Definition 9. Sorting indicator: For a given eigenpair $(\omega_m^\gamma, v_m^\gamma)$, and $l_m, c > 0$, we define the feasible sampling set $X_m := \{x \in \Omega_0 : \inf_{y \in \Omega_r} |x - y| > l_m \text{ and } |v_m(x)| > c\}$, and set

$$\tilde{\delta}_m := \max_{x \in X_m} \tilde{\delta}_m(x), \quad \text{with} \quad \tilde{\delta}_m(x) := |v_m(x) - K v_m(x)|. \tag{40}$$

Due to the rapid growth of eigenfunctions, we expect that non-convergent/spurious pairs exhibit $\beta_m < \alpha_l$. Then, for identification of spurious pairs, it is convenient to compute first the α_l , as suggested in Definition 9.

Remark 10. The proposed strategy consists of evaluating the residual $|(T^\gamma(\omega^\gamma)u^\gamma)(x)|$ in points $x \in X_m$ as suggested by (40). Typically, $N_s \approx 10$ scattered evaluations is sufficient for practical computations. Additionally, we want to exclude points x_l , such that $|u^\gamma(x_l)| \approx 0$, and we want to avoid integrating over cells with a singular kernel. For this, we select points $x_j \notin \Omega_r$ such that $\inf_{y \in \Omega_r} |x_j - y| \geq l_m$, in order to avoid the singularity. Consecutively, we select l_m such that $|\Phi(\omega_m l_m)| \leq C_1$, which guarantees that the integrand is bounded. Ultimately, we use the normalization $v_m := u_m / \|u_m\|_\Omega$, with $\Omega := \Omega_a \cup \Omega_{PML}$ for the PML formulations. Then, we filter out added PML eigenvalues described in Definition 6 by the condition $\|v_m(x)\|_{\Omega_a} / |\Omega_a| > \|v_m\|_{\Omega_{PML}} / |\Omega_{PML}|$.

7.8. Alternative strategies

The identification of spurious pairs in resonance computations has been attempted using a sensitivity approach [46, 47, 48]. The approach is based on the observation that spurious eigenvalues are sensitive to parameter perturbations, while well approximated resonances are not. Approximations of scattering resonances are computed several times with different parameter values (a, σ_0, ℓ) and compared. An disadvantage with the approach is that it only gives a relative measure between eigenvalues with small and with large displacement. Furthermore, the parameter values (a, σ_0, ℓ) changes the accuracy of the eigenvalues. It is therefore not clear when a solution should be marked as spurious, but this approach has nevertheless successfully been used to identify true scattering resonances in small regions of the complex plane. Additionally, the method is expensive as it requires computation of all eigenpairs in a spectral window several times, from where re-meshing and re-assembling of the FE must be performed.

The proposed sorting strategy utilizes Definition 9 for testing each eigenpair on an already assembled FE mesh. The computation re-uses the pre-computed FE environment, the testing has low memory requirements, and the algorithm is fully parallelizable.

7.9. Numerical pseudospectra computation

Computations of the *pseudospectra* provide insight into the behavior of the resolvent of the discretized operator F^γ , allowing us to evaluate its spectral stability. In our computations, we use that $\sigma_\delta(F^\gamma)$ is the set of all $z \in \mathbb{C}$ such that

$$s_{\min} F^\gamma(z) < \epsilon, \quad (41)$$

where $s_{\min} F^\gamma(z)$ denotes the smallest singular value of $F^\gamma(z)$ [1, Definition 2.10]. For the singular value computations we used SLEPc [44].

8. Applications to metal-dielectric nanostructures

In this section we study four interesting configurations, from where numerical approximations to scattering resonances and scattering resonant modes are computed. Consecutively, eigenpairs are tested and solutions are sorted according to their corresponding pseudospectrum indicator (40). The sorting strategy is tested on problems where exact pairs are known. Additionally, we consider a test case used in [48].

The first three configurations serve as benchmarking strategies for non-dispersive and piecewise constant material properties. Then, we apply the sorting algorithm to a configuration introduced in [42] where a metal coating is motivated from realistic applications in nano-photonics. Here, three different relative permittivity models are used: $\epsilon_v := 1$ (*Vacuum*), $\epsilon_s := 2$ (*Silica*), and ϵ_{metal} (*Gold*), modeled by a sum of Drude-Lorentz terms (7). For ϵ_{metal} we use (7) with the data given in Table 3 gathered in [49]. This model of Gold has been extensively tested and has validity for $\omega \in [0.5, 6.5] \text{ eV}$, where *eV* denotes *electron volt*.

We introduce a demanding configuration where the refractive index is a continuous function of space motivated from the so-called *graded materials*. Finally, we consider an acoustic benchmark problem in \mathbb{R}^3 .

$\epsilon_\infty = 1$	$\omega_p = 9.03$	-
$f_0 = 0.76$	$\omega_0 = 0$	$\gamma_0 = 0.053$
$f_1 = 0.024$	$\omega_1 = 0.415$	$\gamma_1 = 0.241$
$f_2 = 0.01$	$\omega_2 = 0.83$	$\gamma_2 = 0.345$
$f_3 = 0.071$	$\omega_3 = 2.969$	$\gamma_3 = 0.87$
$f_4 = 0.601$	$\omega_4 = 4.304$	$\gamma_4 = 2.494$
$f_5 = 4.384$	$\omega_5 = 13.32$	$\gamma_5 = 2.214$

Table 3: Drude Lorentz data (7) for Gold, taken from [49], with time convention $e^{-i\omega t}$.

8.1. Modeling details

In finite precision arithmetic we prefer to work with dimensionless quantities, where we transform from dimensionless variables to physical variables (denoted with \sim). We use common physical constants in SI units: \hbar is the scaled Planck's constant, c is the speed of light in vacuum, and e is the electron charge. In the numerical computations, we use the scaling factors $W = eV/\hbar$ in *Hertz* and $L = 2\pi c/W$ in *meters*. Then, we define the dimensionless quantities

$$x = \frac{\tilde{x}}{L}, \quad \omega = \frac{\tilde{\omega}}{W} \quad \text{satisfying} \quad LW = 2\pi c. \quad (42)$$

The resulting length factor is $L = 1239.842 \text{ nm}$, from where our spectral window becomes numerically equivalent to eV scaling.

8.2. Benchmark in 1D: Slab problem

In [3] we introduced a sorting strategy based on Definition 5 but performed computations only inside Ω_r . As suggested by (32) and (40), computations can be also performed in Ω_0 , and it is natural to ask whether the sorting scheme performs worse if air is included in the evaluation. Then, we numerically test the solutions to the LS formulation by enlarging the computational domain to include air. If the LS would exhibit undesired spurious eigenvalues, this would render the method unreliable for detection of spurious pairs.

The following problem has been considered by several authors including [50, 20]. Define for $n_1 \neq 1$ the piecewise constant function n as

$$n(x) = \begin{cases} n_1 & \text{if } |x| \leq 1, \\ 1 & \text{if } |x| > 1 \end{cases} \quad (43)$$

The corresponding exact resonances of (12)-(13) for the TM polarization are given by

$$e^{4in_1\omega} = \mu^2, \quad \omega_m = \frac{\pi m - i\text{Log}(\mu)}{2n_1}, \quad \mu = \frac{n_1 + 1}{n_1 - 1}. \quad (44)$$

Results: The stability of the spectrum of the DtN, PML, and LS formulations is considered by numerically study the behavior of the computed eigenvalues for perturbations of the domain Ω_a . An essential difference from the experiment presented in [3, Figs 4.1, 5.2, 5.5] is that larger domains $\Omega_a \supseteq \Omega_r$ are used in the computation of (26). The eigenvalues and the pseudospectrum of FE approximations are computed for the slab problem described in Section 8.2 using the tools introduced in Section 7.9. For each formulation, we compare the number of eigenvalues in a fixed region of the complex plane, and the location of eigenvalues that remain in proximity for

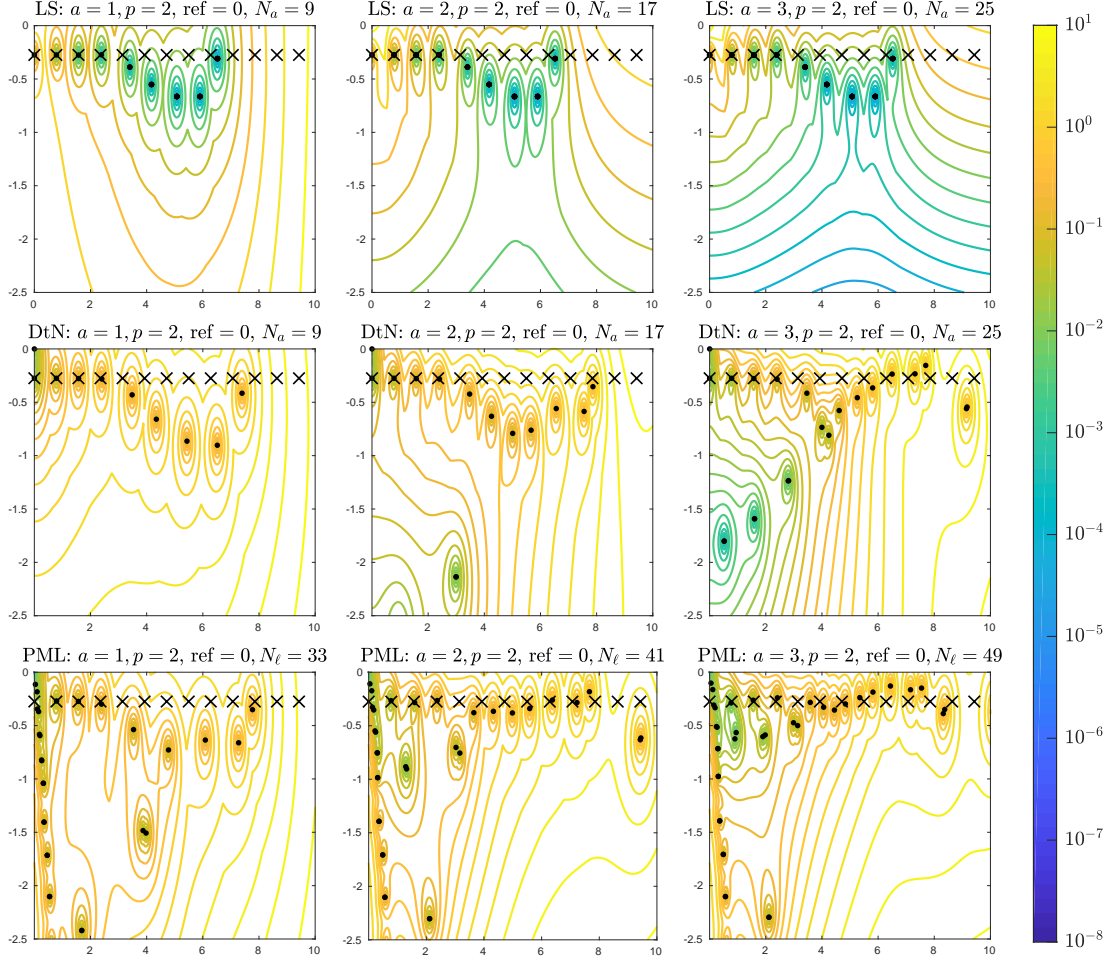


Figure 2: *Pseudospectrum for the TM Slab problem: We illustrate for discretizations with fixed p, h, ℓ the effect of including air regions for the DtN, PML and Lippmann-Schwinger formulations. For reference, we mark with crosses (\times) exact eigenvalues.*

$a = 1, 2, 3$. Note that if the discretization in (26) inherits the property described in Remark 1, then it is expected that the spectrum of the LS formulation would not be sensitive to perturbations of a . The LS formulation is numerically not sensitive to perturbations of the domain, since Figure 2 and Figure 3 shows that no spurious eigenvalues are added, and the computed eigenvalues does not change when increasing a .

We now present the corresponding results for the DtN and the PML formulations. Figures 2 and Figure 3 show that the number of computed eigenvalues increases for increasing a and the locations of the eigenvalues are perturbed. These observations lead us to conclude that the eigenvalues of the DtN and PML formulations are very sensitive to perturbations of the domain.

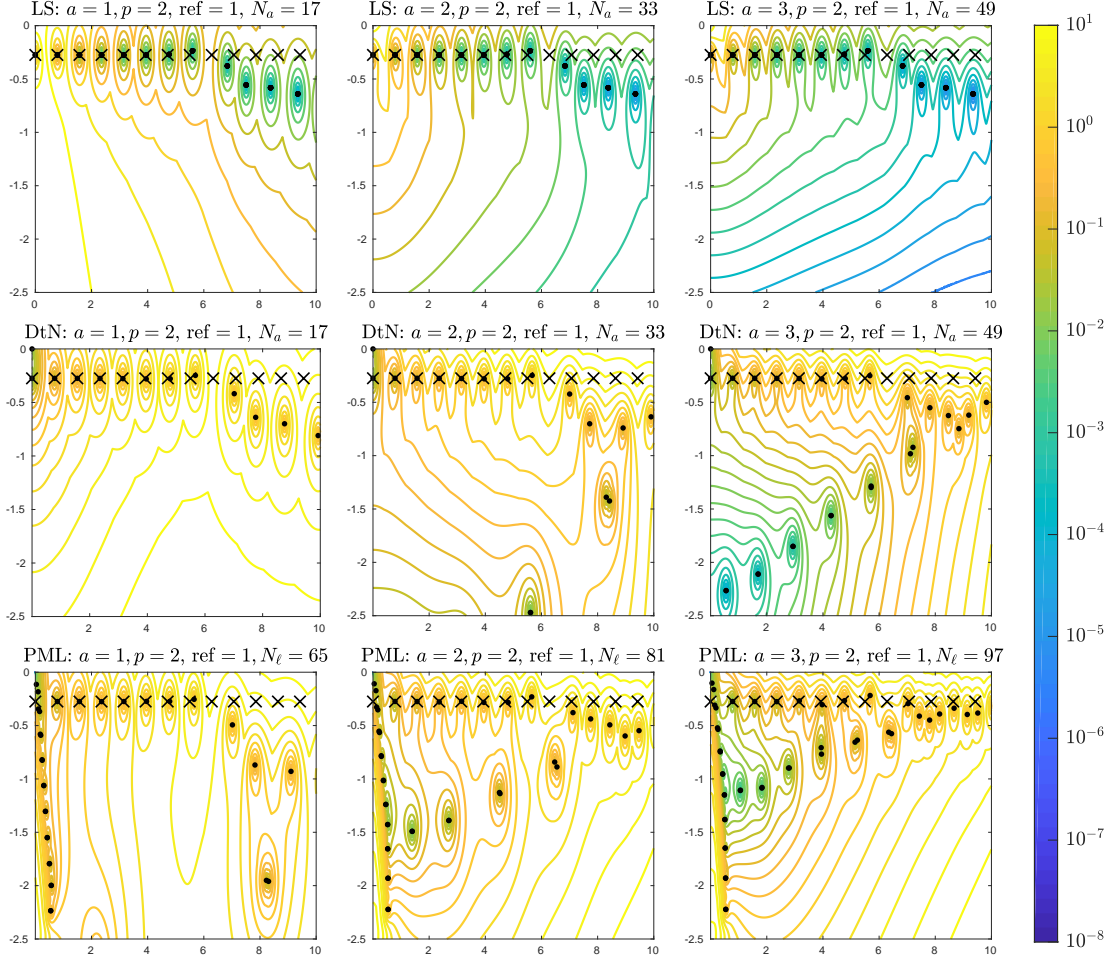


Figure 3: *Pseudospectrum for the TM Slab problem: We illustrate for discretizations with fixed p, h, ℓ the effect of including air regions for the DtN, PML, and Lippmann-Schwinger formulations. For reference, we mark with crosses (\times) exact eigenvalues.*

8.3. Benchmarks in 2D

The next two problems have radial symmetry centered at the origin, and the solutions expressed in polar coordinates (r, θ) , will be written in terms of Bessel and Hankel functions of integer order m . In this simple case outgoing solutions of (9) satisfy

$$u = H_m^{(1)}(a\omega) \begin{pmatrix} \cos m\theta \\ \sin m\theta \end{pmatrix}, \text{ for } x \in \partial B(0, a), \text{ and } m \in \mathbb{Z}, \quad (45)$$

where $\text{supp}(n-1) \subset \Omega_a$. In Subsections 8.3.1 and 8.3.3, we present solutions satisfying (9) and (45) for specific permittivity profiles.

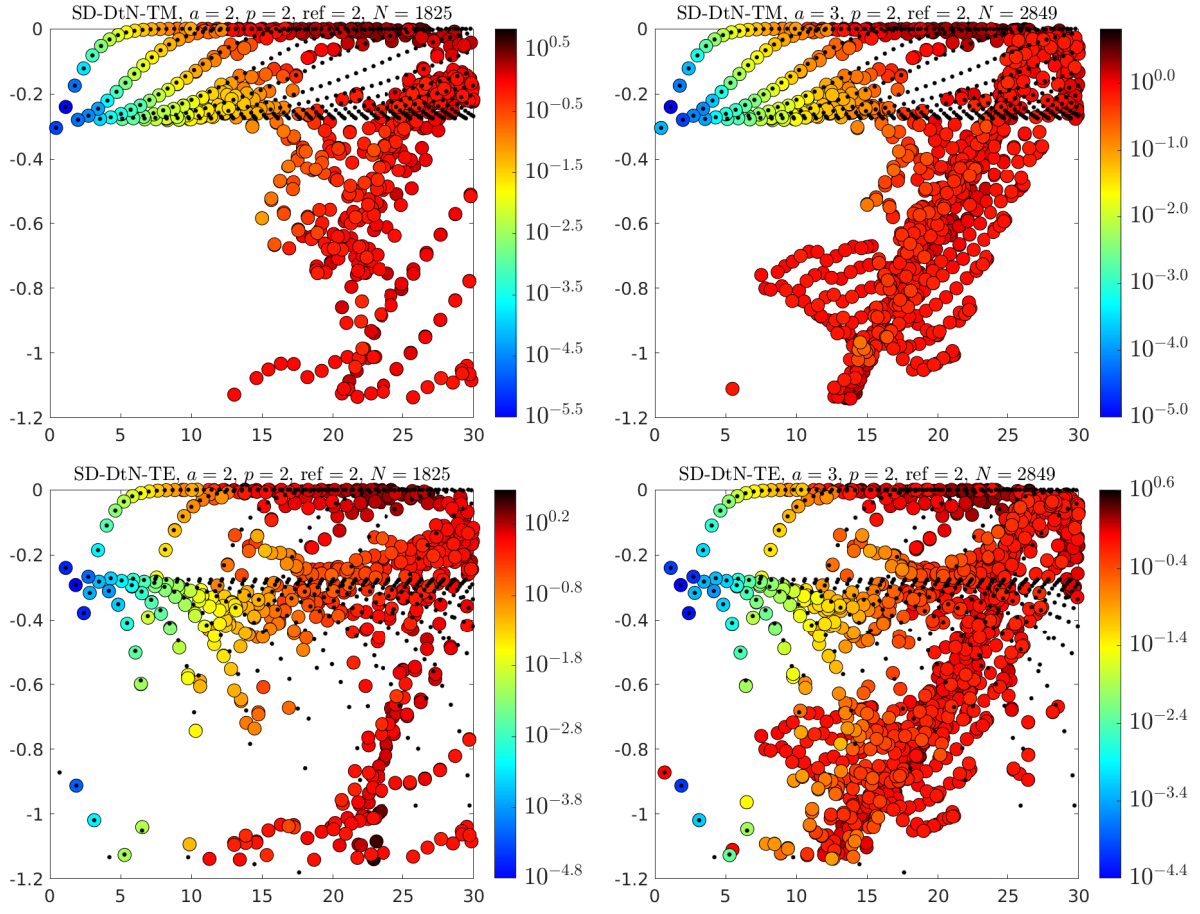


Figure 4: Spectral window showing exact (dots) and FE eigenvalues (circles) the problem described in Section 8.3.1 for TM and TE polarizations. In colors we give $\tilde{\delta}_m$, defined in (40), corresponding to ω_m^γ from computations over ten points.

8.3.1. The single disk problem (SD)

Denote by u_1, n_1 the restrictions of u, n to $\Omega_1 := B(0, R)$, and set $n = n_2 = 1$ elsewhere. The corresponding exact eigenfunctions to (9) and (45) read:

$$u_1 = N_m J_m(n_1 \omega r) \begin{pmatrix} \cos m\theta \\ \sin m\theta \end{pmatrix}, \quad u_2 = H_m^{(1)}(\omega r) \begin{pmatrix} \cos m\theta \\ \sin m\theta \end{pmatrix}, \quad N_m := \frac{H_m^{(1)}(\omega R)}{J_m(n_1 \omega R)}. \quad (46)$$

The eigenvalues ω corresponding to $m = 0$ are *simple* and those corresponding to $m > 0$ are *semi-simple* and have multiplicity $\alpha = 2$. The exact eigenvalue relationship for TM and TE can be written as

$$J_m(n_1 \omega R) H_m^{(1)'}(\omega R) - g J_m'(\omega R) H_m^{(1)}(\omega R) = 0, \quad (47)$$

where $g = n_1, g = 1/n_1$ corresponds to the TM polarization and TE polarization, respectively. For numerical computations we use $R = 1$, and $a = 2, 3$. Additionally, we place the disk center a distance $s = 0.2$ from the origin such that that many terms are needed in the DtN for approximation of resonances.

Results: The application of the sorting scheme (9) to this problem give the results presented in Figure 4. Exact eigenvalues are marked with dots and computed eigenvalues are marked with colored circles, where the color is given by the sorting indicator (40). The upper panels present plots for the TM polarization and in the lower panels results for the TE polarization. The left panels are computed by placing the DtN at $a = 2$, while $a = 3$ in the panels on the right. For both discretizations, the same FE in $B(0, 2)$ is identical.

From the figure we observe that increasing a results in an increase in the number of eigenvalues in the given spectral window, which is expected from the discussion in Section 8.2. Moreover, the added eigenvalues from $a = 3$ pollute larger regions in the spectral window compared to $a = 2$. This conclusion can also be obtained by noticing that the minimum in $\tilde{\delta}$ increases for larger a , which is related to the fact that exponential growth of eigenfunctions become a challenge for FE discretizations. Additionally, we see that the values with small indicator values resemble the pattern drawn by the exact eigenvalues. As the value of the indicator increases the corresponding eigenvalues loose this property and become erratic. It should be noted that the indicator $\tilde{\delta}$ increases with $\text{Re} \omega_m$, which is the expected behavior for the FE discretization error of non-dispersive Helmholtz problems [10, 51, 42]. Additionally, eigenvalues with small indicator values appear very close to the exact eigenvalues of the problem.

8.3.2. The single square problem (SS)

For this problem, we set $\Omega_1 := [-s, s]^2$, $n = n_1$ for $x \in \Omega_1$ and $n = 1$ elsewhere. The correct parameters for obtaining the results presented in [48, Fig. 10] are $s = 1.5$ and $n_1 = 0.2$ for TM polarization.

Results: For this problem, we compute all eigenvalues in the spectral window only once, and test each computed eigenpair. The results are plotted in Figure 5, using a DtN in the left panel, and a PML in the right panel. Both formulations use the same FE basis in Ω_a and we can also in this case see the effectiveness of using the indicator $\tilde{\delta}$. Correct approximations to scattering resonances are easily identified from the overwhelming rest of computed eigenvalues. Additionally, the FE-DtN produces better approximations to scattering resonances than the FE-PML, with lower values on the indicator $\tilde{\delta}_m$ in (40). For example, the two reference values given in [48, Fig. 9] are in Figure 5 marked with dots and it can for those values be seen that $\tilde{\delta}_m$ is smaller for the DtN approach. Comparison of the results in Figure 5 and those in [48, Figs. 10, 11, 12] not

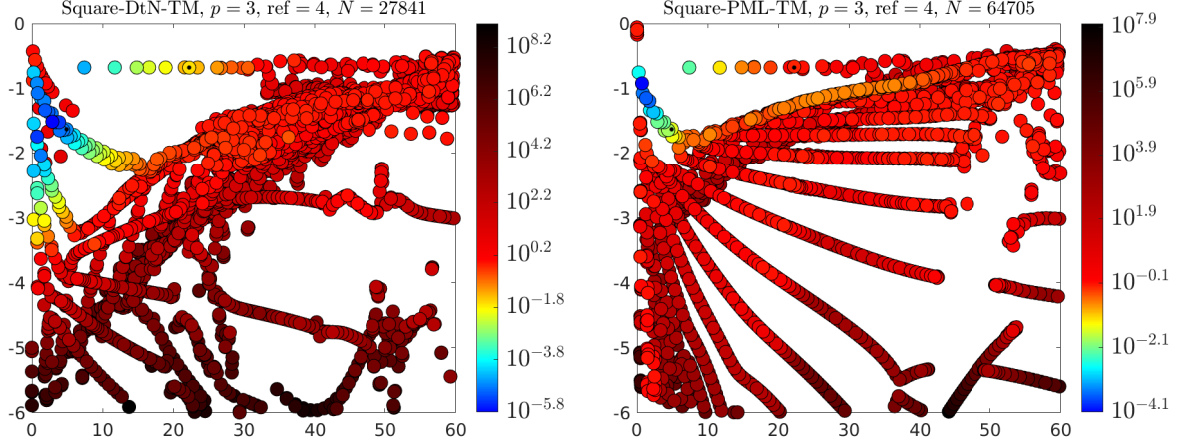


Figure 5: Spectral window showing two reference eigenvalues (dots) from [48] and FE eigenvalues (circles) of the Single Square problem described in Section 8.3.2 for TM polarization. In colors we give $\tilde{\delta}_m$, defined in (40), corresponding to ω_m^γ from computations over ten points.

only illustrates the reliability of the identification of true approximation to resonances by using the scheme in Definition 5, but it also shows its simplicity, flexibility, and large coverage in the complex plane.

8.3.3. Benchmark with dispersion: Single coated disk problem (SCD)

In this configuration, we consider a resonator consisting of a dielectric disk with a uniform coating layer. The geometry is described by two concentric circumferences of radii R_1, R_2 , with $0 < R_1 < R_2$, with vacuum as surrounding medium. The inner disk has constant relative permittivity index, and is coated by a layer of gold. We define $n_1 = \sqrt{\epsilon_s}$ and $n_2 := \sqrt{\epsilon_{metal}}$ such that $\text{Im}\{n_2\}$ (the absorption coefficient) is positive.

The exact solutions satisfy (9), and (45) for $R \geq R_2$. Then, the resonance relationship reads

$$\begin{aligned}
 f_1^m(\omega) &= g_1 J_m'(\omega n_1 R_1) H_m^{(1)}(\omega n_2 R_1) - g_2 J_m(\omega n_1 R_1) H_m^{(1)'}(\omega n_2 R_1), \\
 f_2^m(\omega) &= g_3 J_m(\omega n_1 R_1) H_m^{(2)'}(\omega n_2 R_1) - g_4 J_m'(\omega n_1 R_1) H_m^{(2)}(\omega n_2 R_1), \\
 f_3^m(\omega) &= g_5 H_m^{(1)}(\omega n_2 R_2) H_m^{(1)'}(\omega R_2) - g_6 H_m^{(1)'}(\omega n_2 R_2) H_m^{(1)}(\omega R_2), \\
 f_4^m(\omega) &= g_7 H_m^{(1)}(\omega R_2) H_m^{(2)'}(\omega n_2 R_2) - g_8 H_m^{(1)'}(\omega R_2) H_m^{(2)}(\omega n_2 R_2), \\
 F_m(\omega) &:= (f_1^m f_4^m - f_2^m f_3^m)(\omega) = 0,
 \end{aligned} \tag{48}$$

where for TM, $g := (n_1, n_2, n_2, n_1, 1, n_2, n_2, 1)$, and for TE, $g := (n_2, n_1, n_1, n_2, n_2, 1, 1, n_2)$. The parameters used for the computation are $R_1 = 0.8$, $R_2 = 1.0$ with scaling factor $L = 1239.842 \text{ nm}$.

A complex Newton root finder [52] is then used to compute very accurate approximations of the resonances. For each m in equation (48), we search numerically the resonances $\omega_{m,1}, \omega_{m,2}, \dots$ with machine precision stopping criterion. In [42, Table 2], we list a selection of resonances computed from (48).

Results: The results for both polarizations are gathered in Figure 6. Here, we observe typical behavior of dispersive resonators *i*) there exist clustering of eigenvalues close to the poles and zeros of the Drude-Lorentz model (7), *ii*) in the TE polarization we have clustering of eigenvalues to the

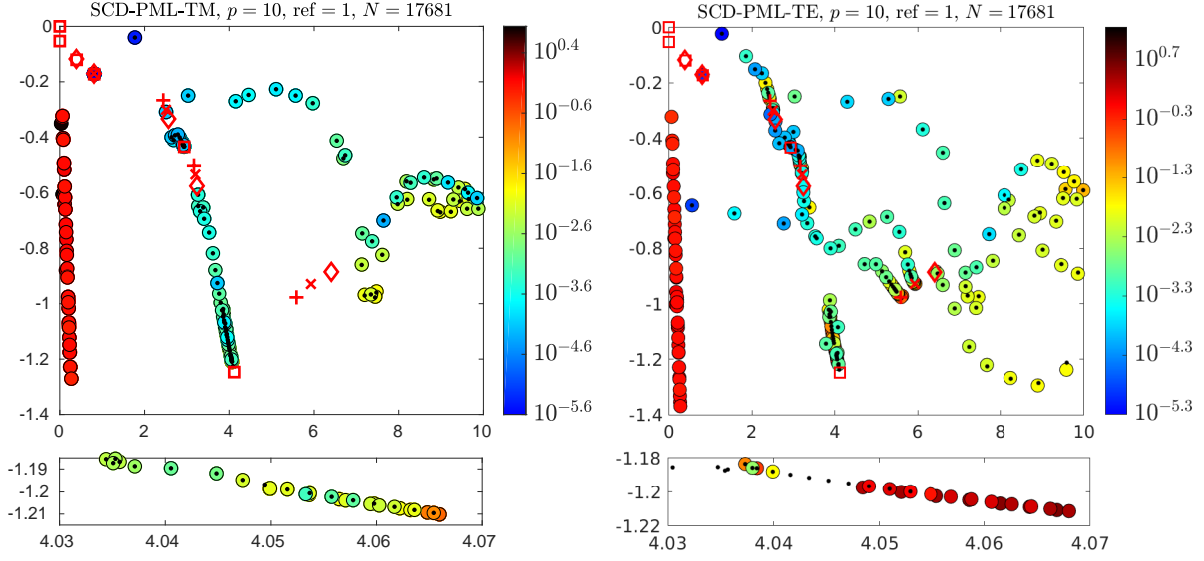


Figure 6: Spectral window showing exact \bullet and FE eigenvalues \circ of the Single Coated Disk problem described in Section 8.3.3 for TM and TE polarizations. The poles of $\epsilon(\omega)$ are given by \square and its roots $\epsilon(\omega) = 0$ with \diamond . Additionally, the plasmonic branch points $\epsilon(\omega) = -1$ is marked with (\times) , and $\epsilon(\omega) = -2$ with $(+)$. In colors we give $\tilde{\delta}_m$, defined in (40), corresponding to ω_m^j from computations over ten points.

so-called *plasmonic branch points* of the model, which are those values ω such that $\epsilon_{\text{metal}}(\omega) = -\epsilon_j$, with $j = 0, 1$. In other words, $-\epsilon_{\text{metal}}(\omega)$ matches the value of a neighboring dielectric constant (juncture). In the figure, the bottom panels are close up windows showing such accumulations and the corresponding values for the resulting eigenpair indicator $\tilde{\delta}_m$. As expected, the value of $\tilde{\delta}_m$ increases when approaching a critical value (pole, or zero). This behavior is expected since close to a critical point the value $|n(\omega)\omega|$ increases and the resulting eigenfunction oscillates more rapidly, which implies that the FE error increases. This is further discussed in [42].

8.3.4. Configuration with continuous $n(x)$: Bump problem

Consider the following refractive index:

$$n(x) = \begin{cases} 1 + P_3(|x|) & 0 \leq |x| \leq R \\ 1 & |x| > R \end{cases} \quad (49)$$

subject to the compatibility conditions: $P_3(0) = 1$, $P_3(R) = 0$, $P_3'(0) = 0$, $P_3'(R) = 0$, and $R = 1$. *Results:* Figure 7 illustrate the application of the sorting scheme in Definition 9 to a configuration with graded material properties .

9. Applications to Acoustics

In this section we consider acoustic sound-soft resonators in \mathbb{R}^3 . The acoustic pressure u satisfies then formally the Helmholtz equation (4).

9.1. Acoustic benchmark in 3D: Single ball problem (SB)

This case is analogous to the Single Disk problem in Section 8.3.1 with $d = 3$. Denote by $u = u_1$, $n = n_1$ the restrictions of u, n to $\Omega_1 := B(0, R)$, and set $n = n_2 = 1$ elsewhere. We denote

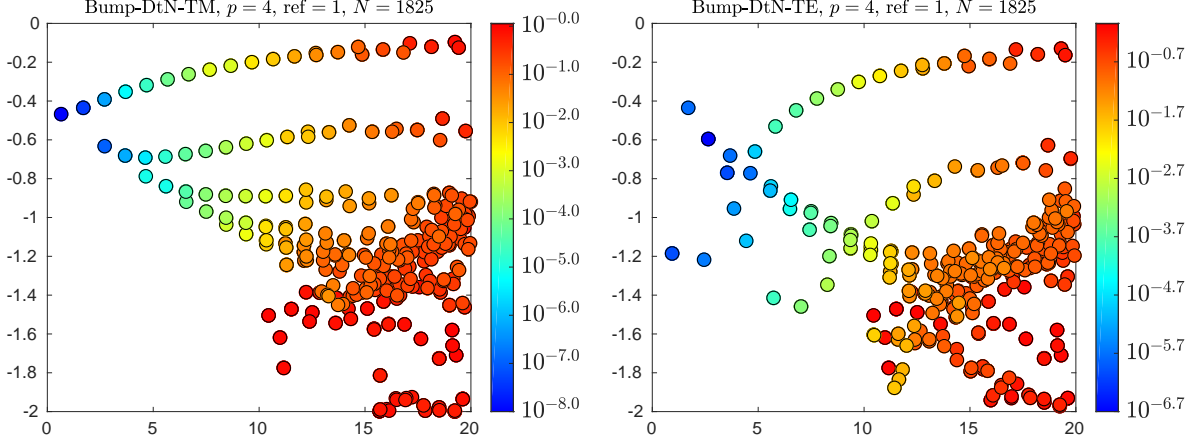


Figure 7: Spectral window showing computed FE eigenvalues (circles) of the Bump problem described in Section 8.3.4 for TM and TE polarizations. In colors we give $\tilde{\delta}_m$, defined in (40), corresponding to ω_m^γ from computations over ten points.

by $j_m(x)$ and $h_m^{(1)}(x)$ the spherical Bessel and Hankel functions of the first kind, and by Y_ℓ^m the Spherical harmonics. The corresponding exact outgoing resonant modes of (9) read:

$$u_{m\ell}(r, \theta, \phi) = \begin{cases} N_m j_m(n_1 \omega r) Y_\ell^m(\theta, \phi), & r \leq R \\ h_m^{(1)}(\omega r) Y_\ell^m(\theta, \phi), & r > a \end{cases}, \quad |\ell| < m, \quad N_m := \frac{h_m^{(1)}(\omega R)}{j_m(n_1 \omega R)}. \quad (50)$$

The eigenvalues ω corresponding to $m = 0$ are *simple* and those corresponding to $m > 0$ are *semi-simple* and have multiplicity $\alpha = 2m + 1$. The exact eigenvalue relationship can be written as

$$j_m(n_1 \omega R) h_m^{(1)\prime}(\omega R) - n_1 j_m'(\omega R) h_m^{(1)}(\omega R) = 0. \quad (51)$$

Results: Figure 8 confirms the positive results from the application of the sorting scheme in Definition 9 to several test cases in electromagnetics. The FE matrices are denser for $d = 3$ compared with $d = 2$, which results in a high demand of memory per used shift. Additionally, multiplicities are in general larger when $d = 3$, which implies that it is necessary to increase the number of Krylov vectors for the computation of a given number of different eigenvalues. This results in a high demand in memory, e.g. in our test case ARPACK used 28 Gb of ram for each shift for the computation of ten eigenpairs.

The results in the figures illustrate a clear method to sort the computed eigenpairs by using the pseudospectrum indicator (40) effectively, which then can be used to remove pairs with $\tilde{\delta}_j > \delta_{TOL}$, where δ_{TOL} is a chosen threshold.

10. Conclusions

We have presented a sorting scheme, based on the Lippmann–Schwinger equation, for the removal of spurious scattering resonant pairs in \mathbb{R}^d Helmholtz problems. Numerical experiments on a broad range of benchmarks illustrate that the sorting scheme can be used to give valuable information on the location of true resonances at low computational cost.

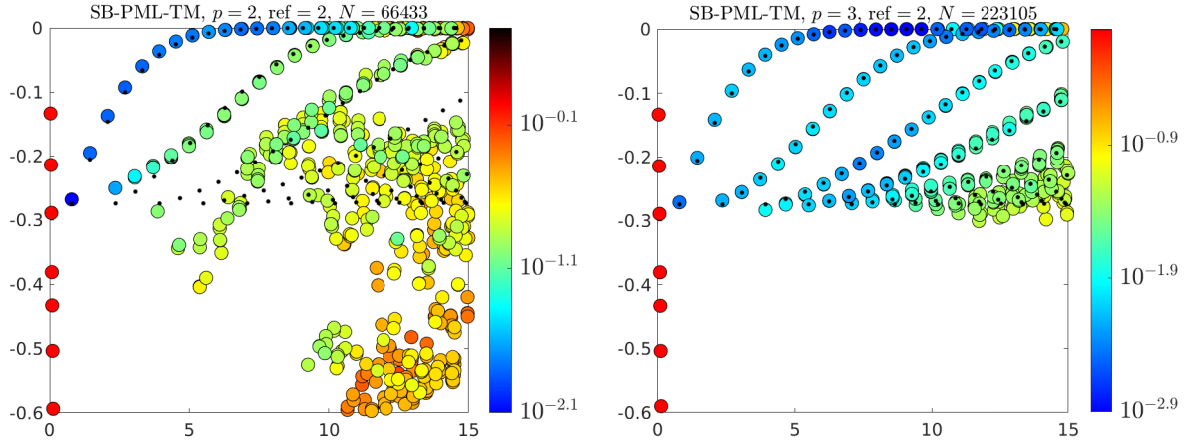


Figure 8: Spectral window showing exact (dots) and FE eigenvalues (circles) the Single Ball problem described in Section 9.1 for TM and TE polarizations. In colors we give δ_m , defined in (40), corresponding to ω_m^γ from computations over ten points.

Acknowledgments

This work is funded by the Swedish Research Council under Grant No. 621-2012-3863.

References

- [1] Lloyd N. Trefethen and Mark Embree. *Spectra and Pseudospectra: The Behavior of Nonnormal Matrices and Operators*. Princeton University Press, July 2005.
- [2] E. B. Davies. Pseudospectra of differential operators. *J. Oper. Th.*, 43:243–262, 1997.
- [3] J. C. Araujo C. and C. Engström. On spurious solutions in finite element approximations of resonances in open systems. *Computers & Mathematics with Applications*, 74(10):2385 – 2402, 2017.
- [4] M. Cessenat. *Mathematical Methods in Electromagnetism*. Series on Advances in Mathematics for Applied Sciences — Vol. 41. World Scientific Publisher, Singapore, 1996.
- [5] R. B. Melrose. *Geometric scattering theory*. Stanford Lectures. Cambridge University Press, Cambridge, 1995.
- [6] Peter D. Lax and Ralph S. Phillips. *Scattering theory*, volume 26 of *Pure and Applied Mathematics*. Academic Press, Inc., Boston, MA, second edition, 1989. With appendices by Cathleen S. Morawetz and Georg Schmidt.
- [7] J. Gopalakrishnan, S. Moskow, and F. Santosa. Asymptotic and numerical techniques for resonances of thin photonic structures. *SIAM Journal of Applied Mathematics*, 69(1):37–63, 2008.
- [8] Braxton Osting and Michael I. Weinstein. Long-lived scattering resonances and bragg structures. *SIAM Journal of Applied Mathematics*, 73(2):827–852, 2013.
- [9] Chiu-Yen Kao and Fadil Santosa. Maximization of the quality factor of an optical resonator. *Wave Motion*, 45(4):412–427, 2008.
- [10] F. Ihlenburg. *Finite element analysis of acoustic scattering*. Applied mathematical sciences. Springer, New York, 1998.
- [11] X. Wang, Y. Deng, Q. Li, Y. Huang, Z. Gong, K.B. Tom, and J. Yao. Excitation and propagation of surface plasmon polaritons on a non-structured surface with a permittivity gradient. *Light Sci. Appl.*, 5(12), 2016.
- [12] Olaf Steinbach and Gerhard Unger. Combined boundary integral equations for acoustic scattering-resonance problems. *Math. Methods Appl. Sci.*, 40(5):1516–1530, 2017.
- [13] Thorsten Hohage and Lothar Nannen. Hardy space infinite elements for scattering and resonance problems. *SIAM J. Numer. Anal.*, 47(2):972–996, 2009.
- [14] J. C. Araujo C., C. Engström, and E. Jarlebring. Efficient resonance computations for Helmholtz problems based on a Dirichlet-to-Neumann map. *Journal of Computational and Applied Mathematics*, 330:177 – 192, 2018.

- [15] Elias Jarlebring, Karl Meerbergen, and Wim Michiels. Computing a partial schur factorization of nonlinear eigenvalue problems using the infinite arnoldi method. *SIAM Journal on Matrix Analysis and Applications*, 35(2):411–436, 2014. QC 20140908.
- [16] E. Jarlebring, G. Mele, and O. Runborg. The waveguide eigenvalue problem and the tensor infinite Arnoldi method. *ArXiv e-prints*, March 2015.
- [17] E. B. Davies. Non-self-adjoint differential operators. *Bull. London Math. Soc.*, 34(5):513–532, 2002.
- [18] M. Lenoir, M. Vullierme-Ledard, and C. Hazard. Variational formulations for the determination of resonant states in scattering problems. *SIAM J. Math. Anal.*, 23(3):579–608, 1992.
- [19] F. Schenk. *Optimization of Resonances for Multilayer X-ray Resonators*. Göttingen series in x-ray physics. Univ.-Verlag Göttingen, 2011.
- [20] S. Kim and J. E. Pasciak. The computation of resonances in open systems using a perfectly matched layer. *Math. Comp.*, 78(267):1375–1398, 2009.
- [21] James H. Bramble and Joseph E. Pasciak. Analysis of a finite PML approximation for the three dimensional time-harmonic maxwell and acoustic scattering problems. *Math. Comput.*, 76(258):597–614, 2007.
- [22] Yasuhiko Ikebe. The galerkin method for the numerical solution of fredholm integral equations of the second kind. *SIAM Review*, 14(3):465–491, 1972.
- [23] Junko Asakura, Tetsuya Sakurai, Hiroto Tadano, Tsutomu Ikegami, and Kinji Kimura. A numerical method for nonlinear eigenvalue problems using contour integrals. *JSIAM Lett.*, 1:52–55, 2009.
- [24] W-J. Beyn. An integral method for solving nonlinear eigenvalue problems. *Linear Algebra Appl.*, 436(10):3839–3863, 2012.
- [25] Christian Engström and Luka Grubišić. A subspace iteration algorithm for Fredholm valued functions. *Math. Probl. Eng.*, pages Art. ID 459895, 14, 2015.
- [26] I. Babuška and B. Q. Guo. The h, p and h-p version of the finite element method: Basis theory and applications. *Adv. Eng. Softw.*, 15(3-4):159–174, November 1992.
- [27] C. Schwab. *p- and hp- Finite Element Methods: Theory and Applications in Solid and Fluid Mechanics*. Oxford University Press, 1998.
- [28] Gilbert Strang and George Fix. *An analysis of the finite element method*. Wellesley-Cambridge Press, Wellesley, MA, second edition, 2008.
- [29] P. Solin, K. Segeth, and Ivo D. *Higher-order finite element methods*. Studies in advanced mathematics. Chapman & Hall/CRC, Boca Raton, London, 2004.
- [30] William J. Gordon and Charles A. Hall. Transfinite element methods: Blending-function interpolation over arbitrary curved element domains. *Numerische Mathematik*, 21(2):109–129, Apr 1973.
- [31] William J. Gordon and Charles A. Hall. Construction of curvilinear co-ordinate systems and applications to mesh generation. *International Journal for Numerical Methods in Engineering*, 7(4):461–477, 1973.
- [32] J. T. Oden and J. N. Reddy. *An introduction to the mathematical theory of finite elements*. Wiley-Interscience [John Wiley & Sons], New York-London-Sydney, 1976. Pure and Applied Mathematics.
- [33] Begnaud Francis Hildebrand. *Introduction to Numerical Analysis: 2Nd Edition*. Dover Publications, Inc., New York, NY, USA, 1987.
- [34] P. Solin, K. Segeth, and I. Dolezel. *Higher-order finite element methods*. Studies in advanced mathematics. Chapman & Hall/CRC, Boca Raton, London, 2004.
- [35] G. Alzetta, D. Arndt, W. Bangerth, V. Boddu, B. Brands, D. Davydov, R. Gassmoeller, T. Heister, L. Heltai, K. Kormann, M. Kronbichler, M. Maier, J.-P. Pelteret, B. Turcksin, and D. Wells. The `deal.II` library, version 9.0. *Journal of Numerical Mathematics*, 26(4):173–183, 2018.
- [36] D. Colton and R. Kress. *Integral Equation Methods in Scattering Theory*. John Wiley & Sons, New York, 1983.
- [37] Hideaki Kaneko and Yuesheng Xu. Gauss-type quadratures for weakly singular integrals and their application to Fredholm integral equations of the second kind. *Math. Comp.*, 62(206):739–753, 1994.
- [38] Ran Duan and Vladimir Rokhlin. High-order quadratures for the solution of scattering problems in two dimensions. *Journal of Computational Physics*, 228(6):2152 – 2174, 2009.
- [39] B.V. Rathish Kumar A. Anand, A. Pandey and J. Paul. An efficient high-order nyström scheme for acoustic scattering by inhomogeneous penetrable media with discontinuous material interface. *Journal of Computational Physics*, 311:258 – 274, 2016.
- [40] E. Jarlebring, W. Michiels, and K. Meerbergen. A linear eigenvalue algorithm for the nonlinear eigenvalue problem. 122(1):169–195, 2012.
- [41] E. Jarlebring, G. Mele, and O. Runborg. The waveguide eigenvalue problem and the tensor infinite Arnoldi method. Technical report, KTH Royal Institute of Technology, 2015. arxiv preprint.
- [42] Juan C. Araujo C, Carmen Campos, Christian Engström, and Jose E. Roman. Computation of scattering

- resonances in absorptive and dispersive media with applications to metal-dielectric nano-structures, 2019.
- [43] S. Güttel and F. Tisseur. The nonlinear eigenvalue problem. *Acta Numerica*, 26:1–94, 2017.
 - [44] V. Hernandez, J. E. Roman, and V. Vidal. SLEPc: A scalable and flexible toolkit for the solution of eigenvalue problems. *ACM Trans. Math. Software*, 31(3):351–362, 2005.
 - [45] S. Balay, W. D. Gropp, L. C. McInnes, and B. F. Smith. Efficient management of parallelism in object oriented numerical software libraries. In E. Arge, A. M. Bruaset, and H. P. Langtangen, editors, *Modern Software Tools in Scientific Computing*, pages 163–202. Birkhäuser Press, 1997.
 - [46] B. Kettner and F. Schmidt. The pole condition as transparent boundary condition for resonance problems: detection of spurious modes. In *Physics and Simulation of Optoelectronic Devices XIX*, volume 7933, page 79331B. Proc. SPIE, 2011.
 - [47] Benjamin Kettner. *Detection of spurious modes in resonance mode computations*. PhD thesis, 2012.
 - [48] Lothar Nannen and Markus Wess. Computing scattering resonances using perfectly matched layers with frequency dependent scaling functions. *BIT Numerical Mathematics*, 58(2):373–395, Jun 2018.
 - [49] A. D. Rakić, A. B. Djurišić, J. M. Elazar, and M. L. Majewski. Optical properties of metallic films for vertical-cavity optoelectronic devices. *Appl. Opt.*, 37(22):5271–5283, Aug 1998.
 - [50] Braxton Osting and Michael I. Weinstein. Long-lived scattering resonances and Bragg structures. *SIAM J. Appl. Math.*, 73(2):827–852, 2013.
 - [51] M. Ainsworth. Discrete dispersion relation for hp-version finite element approximation at high wave number. *SIAM Journal on Numerical Analysis*, 42(2):553–575, 2005.
 - [52] A. Ben-Israel L. Yau. The Newton and Halley methods for complex roots. *The American Mathematical Monthly*, 105(9):806–818, 1998.